Ultrasonic-electrodeposition construction of high hydrophobic Ce-PDMS-PbO$_2$/SS electrode for p-nitrophenol degradation: Catalytic, kinetics and mechanism

Huixi Li, Haoran Wu, Linxia Li, Wei Zhu, Shuting Li, Qiang Yu, Lei Han [*], Zhen Chen [*]

Faculty of Science, Kunming University of Science and Technology, Kunming 650500, PR China

ABSTRACT

In this work, a novel hydrophobic microsphere Ce-PDMS-PbO$_2$ structure on stainless steel (SS) was prepared via ultrasonic-electrodeposition as an efficient anodic electrocatalyst for p-nitrophenol (PNP) degradation. Compared to PbO$_2$/SS, such Ce-PDMS-PbO$_2$/SS electrode exhibits obviously lower activation energy (19.20 kJ mol^{-1}) and charge transfer resistance (3.268 Ω cm^{-2}), tolerable stability, higher exchange current density (1.171 $\times 10^{-5}$ A cm^{-2}) and electrochemical active area (202.0 cm^2). The as-synthesized Ce-PDMS-PbO$_2$/SS anode achieved drastically enhanced PNP removal efficiency of 96.9% in 120 min, and the degradation reaction-order was calculated to be 0.9123 conformed to the quasi-first-order reaction kinetics. The GC-MS results reveal the possible PNP degradation pathway under the action of both anodic and cathodic reactions. Furthermore, the DFT calculation results show that Ce doping can decrease the activation energy barrier of ·OH and promote the ·OH generation. Overall, this work offers a new strategy and comprehension to construct a high-efficiency electrode for PNP pollutants degradation.

1. Introduction

The rapid development of industry has led to the discharge of more and more industrial wastewater directly into natural waters. Wastewater, however, contains a large amount of non-biodegradable organic, toxic pollutants. Among these are nitrophenols and their derivatives, which occur in industrial and agricultural wastewater as mutagenic, refractory aromatic pollutants, have drawn much attention for their persistence and high toxicity in the environment [1]. Particularly, p-nitrophenol (PNP) is a key intermediate and raw material in the manufacture of pesticides, dyes, explosives, and wood preservatives [2]. There is no doubt that PNP has many detrimental effects on public health and environment. For instance, exposure to PNP can harm the nervous system, damage blood cells, and cause organisms to become mutated. Due to this, the EPA of the United States has listed it as a priority pollutant [3,4]. Utilizing effective and low-cost pollution control technologies is paramount to eradicating PNP from water environments. Based on the above considerations, PNP was selected as the model pollutant in this study.

For the past few years, advanced oxidation technologies such as catalytic ozonation [5], Fenton oxidation [6], photocatalytic oxidation [7], and supercritical water oxidation [8] have been widely studied in the water and wastewater treatment field. Electrocatalytic oxidation technology has become one of the most attractive advanced oxidation technologies for its remarkable advantages such as environmental friendliness, low cost, safety, and simple operation, especially for non-biodegradable organic and toxic pollutants [9,10]. As we all know, as the key to electrocatalytic oxidation technology, electrode material determines the electrochemical stability and activity of the electrode. Consequently, various types of electrodes, such as Pt, IrO$_2$, RuO$_2$, SnO$_2$, BDD, and PbO$_2$ electrodes, have been investigated in previous research [11]. However, these electrodes have many disadvantages, for instance: the Pt electrode has good corrosion resistance but poor electrocatalytic activity and low current efficiency [12]; the IrO$_2$ and RuO$_2$ electrodes possess not only high price but also low electrocatalytic activity for the organic pollutants oxidation [13]; the SnO$_2$ electrode owns a high oxygen evolution potential but a short service lifetime [14]; and the BDD electrode exhibits high electrocatalytic degradation activity and remarkable stability while relatively high cost [15]. Nevertheless, it's worth noting that the PbO$_2$ electrode owns excellent electrocatalytic performance, long life, good corrosion resistance, and low cost, so it has been widely used in the electrocatalytic oxidation process and is

considered one of the most promising electrocatalytic oxidation anode materials [16,17]. Even so, there also exist some drawbacks such as lead leakage [18], unsatisfactory actual service life [13], etc. that limit its application for water and wastewater treatment, it is urgent to further improve the performance of PbO_2 electrode.

As is well-known, the performance especially the electrocatalytic activity of PbO_2 electrode can usually be improved via several modification strategies [19]. Metal element doping is a common and effective method to modify PbO_2 electrode to enhance its performance. As an important branch of metal element doping, rare earth element doping is widely employed in the modification of PbO_2 electrode, such as Sm [20], Er [21], Ce [22], Pr [23], Yb [24], Nd [25], etc. As a result of the 4f electronic structure of rare earth metal elements, their atoms can easily be polarized and deformed, and then forms holes, vacancies and other defects by filling gaps or replacing with host atoms into the crystal lattice of PbO_2, which may bring great improvements and changes to the performance of PbO_2 electrodes [17]. And Ce is probably the most commonly applied dopant, which provides a new nucleation center for PbO_2, minimizes the internal stress of PbO_2 crystal and enhances the electron transfer ability, thus reducing the PbO_2 average size and hindering its further growth [26,27]. Additionally, several previous studies have revealed that the PbO_2 anode with hydrophobic surface possesses low adsorbability for ·OH, more easily to release ·OH free radicals, thus enhancing the oxygen evolution potential and the utilization rate of ·OH radicals for organics degradation [22,28,29]. Owing to the adsorbed ·OH will cause some side reactions, for instance, oxygen evolution reaction, leading to relatively low amounts of ·OH participating in organic pollutant oxidation [30]. Therefore, it is very desirable to adjust the PbO_2 surface properties from hydrophilic to hydrophobic. As we all know, surfactant and polymer additives can impact the PbO_2 electrodeposition kinetics without changing the process mechanism [31,32]. Through adsorbing on certain surfaces, the additives reduce the growth rate of these surfaces and change the grown crystals shape. Thus increasing the anode surface hydrophobicity and facilitating the reaction between pollutants and PbO_2. Therefore, polymers and surfactants are widely used as additives to improve the anode surface properties, such as polyvinyl alcohol (PVA) [33], polytetrafluoroethylene (PTFE) [34], polyvinylidene fluoride (PVDF) [35], sodium dodecyl benzene sulfonate (SDBS) [36], sodium dodecyl sulfate (SDS) [37], etc were employed to modify the surface of PbO_2 electrode to make it hydrophobic. Among them, as an extensively used hydrophobic polymer, polydimethylsiloxane (PDMS) possesses many outstanding properties, such as hydrophobicity, high shear resistance, chemical corrosion resistance, low cost, and physiological inertia [30,38]. Although PDMS has such advantages, the research on using it as a modifier to change the surface properties of PbO_2 has been rarely reported.

In addition, the common preparation method of β-PbO_2 with high catalytic activity is electrodeposition. And the preparation conditions and deposition methods will impact the morphology, quality and even electrochemical performance of the electrode coating. Among them, the deposition method has a more obvious effect on the quality and performance of PbO_2 coating, for example, compared to the traditional PbO_2 coating obtained from direct current electrodeposition, the electrode coating prepared by pulse electrodeposition is more compact and uniform, and the electrochemical performance is better [39,40]. Additionally, the addition of ultrasonic field in the process of electrodeposition can also have a great influence on the quality and properties of PbO_2 coating [41]. González-García et al. [42] found that the use of ultrasonic field can improve the actual electrodeposition process of lead dioxide and provide uniform, stress-free, and nodular-free thin films on carbon and titanium substrates. Compared with other traditional operating variables, such as current density, temperature, and additives, the existence of ultrasonic wave also greatly promotes the quality of the coating, and the corrosion rate is lower in the accelerated life test reaction. Even so, the study of PbO_2 electrode prepared via ultrasonic-electrodeposition for catalysis and degradation is rare. For

instance, Ni et al. [43] prepared Ti/TiO_2-NTA/PbO_2-La electrode via electrodeposition and employed it to degrade ciprofloxacin at a certain ultrasonic power. While Sáez et al. [44] only prepared PbO_2 on glassy carbon electrode via ultrasonic-electrodeposition without applying it for pollutant degradation.

Herein, we reported a method of preparing hydrophobic Ce-doped PDMS-modified PbO_2 composite electrode on the stainless steel surface via ultrasonic-electrodeposition and applied it for the PNP electrochemical degradation. By introducing Ce^{3+} and PDMS into the electrolyte to modify the active layer of PbO_2, the structure and surface hydrophobicity of the electrode were successfully modulated, thus the PbO_2 anode service life and the electrocatalytic performance for oxidative degradation of PNP were improved. The effects of surface morphology, element composition, and crystal plane orientation on the electrochemical properties of the modified electrode were studied systematically. Additionally, the effect mechanism of different modifiers on the electrocatalytic degradation of PNP by PbO_2 anode was also explored. The electrocatalytic oxidation performance of the prepared Ce-PDMS-PbO_2/SS electrode is closely related to the additives, indicating that metal ion doping and organic polymer modification can effectively change the inherent structure, morphology, hydrophobicity, and electrochemical performance of the PbO_2 electrode. Besides, the PNP electrochemical oxidation mechanism on the Ce-PDMS-PbO_2/SS anode was further discussed by the GC-MS method. Furthermore, the essential reason for the improvement of catalytic performance of PbO_2 by Ce doping was studied via DFT calculation, and the degradation process of PNP on the surface of PbO_2 electrode was theoretically simulated. This work not only provides an attractive PbO_2 anode material for PNP electrocatalytic oxidation but also provides a new way for reasonable design, economic and stable wastewater treatment electrode.

2. Experimental part

2.1. Preparation of electrode materials

2.1.1. Ce-PDMS-PbO$_2$/SS electrode preparation

The Ce-PDMS-PbO_2/SS electrode was prepared via the ultrasonic-electrodeposition method. The pretreated stainless steel sheet (1 cm $\times$ 4 cm) is used as the anode and the stainless steel ring as the cathode. The basic plating bath (200 ml) in a beaker consists of 15 g L^{-1} $Cu(NO_3)_2$, 190 g L^{-1} $Pb(NO_3)_2$, and 0.5 g L^{-1} NaF. And the addition amount of Ce $(NO_3)_3$ and PDMS is 8 mM and 0.8 ml L^{-1}, respectively. The ultrasonic power is 50 W, the current density is 10 mA cm^{-2}, the magnetic stirring speed is 200 rpm, the temperature is 40 ℃, the pH is ~3, and the electrodeposition time is 20 min (The steady-state polarization curve and electrochemical impedance spectroscopy test were used to optimize the ultrasonic power, Ce^{3+} addition, and PDMS addition, as shown in Fig. S1. Under the condition of 50 W ultrasonic power, 8 mM $Ce(NO_3)_3$, and 0.8 ml L^{-1} PDMS, the modified PbO_2 electrode exhibits the best catalytic performance, so the modified PbO_2 electrodes in this paper are all prepared under this optimal condition.).

In addition, the unmodified PbO_2 electrode (hereinafter abbreviated as PbO_2/SS), Ce^{3+} doped PbO_2 electrode (hereinafter abbreviated as Ce-PbO_2/SS) and PDMS modified PbO_2 electrode (hereinafter abbreviated as PDMS-PbO_2/SS) were prepared with the same preparation method and technological conditions, and their related properties were compared. The PbO_2 electrode obtained by direct electrodeposition without ultrasound is referred to as $PbO_2(0)$/SS.

2.2. Physical characterization

The surface morphology and element distribution of the electrode were characterized by scanning electron microscope (SEM, JSM-7800 F). The crystallography information was detected by transmission electron microscopy (TEM, FEI Talos F200s). The crystal structure of the prepared electrode was studied by X-ray diffractometer (CuKA,45 KV,

Japan). The elemental composition and chemical state were analyzed by XPS (Thermo Scientific K-Alpha). The existence of functional groups on the electrode surface was studied by Fourier transform infrared spectroscopy (FT-IR). The contact angle of water on the surface of the electrode was measured by contact angle measuring instrument (DataphysicsOCA30, Germany). A UV–vis spectrophotometer was applied to measure the concentration of PNP using Lambert-Beer law, while the ICP-AES was employed to determine the total Pb concentration after 120 min degradation. Total organic carbon (TOC) was determined using a TOC analyzer (Thermo Scientific Vario TOC). Electron paramagnetic resonance (EPR, Bruker EMXPLUS) was employed to determine the generated active species during the PNP electrocatalytic oxidation on the surfaces of the as-fabricated electrode.

3. Results and discussion

3.1. Physical characterization of the electrodes

3.1.1. Surface morphology analysis and Contact angle test

Various magnification SEM images of PbO_2/SS, Ce-PbO_2/SS, PDMS-PbO_2/SS, and Ce-PDMS-PbO_2/SS electrodes are shown in Fig. 1a-k. As can be seen from Fig. 1a-b, the surface layer of PbO_2 is quasi-pyramid and rough. Through careful observation, some cracks can be found. In contrast, the surface morphology of Ce-PbO_2/SS in Fig. 1d-e changed obviously, from quasi-pyramid structure to spherical particle structure. According to the crystal simulation diagram (Fig. S3), the doping of Ce could vary the crystal structure of PbO_2. As shown in Fig. 1g-h that PDMS modification does not vary the quasi-pyramid morphology of PbO_2, while the grain size is slightly refined. However, the grains of Ce-doped and PDMS-modified PbO_2 in Fig. 1j-k illustrate a uniform "black bean" particle shape, and the grains are more refined than that of Ce-PbO_2/SS. In addition, the surface roughness test images (Fig. S4) and results (Table S1) reveal that both Ce doping and PDMS modification can refine the PbO_2 grains, and the PbO_2 grains co-modified by Ce and PDMS show the minimum grain size. Moreover, the surface grain size of PbO_2(0)/SS electrode prepared by electrodeposition without ultrasonic treatment is larger and uneven than that of PbO_2/SS electrode (Fig. S5), which implies that the treatment of ultrasonic field with appropriate power in the electrodeposition process is beneficial to the preparation of PbO_2/SS electrode surface with uniform size and small grains.

The effects of Ce doping and PDMS modification on the wettability of PbO_2/SS electrode were studied by contact angle measurement. The contact angle of PbO_2/SS electrode is 81.3°(inset in Fig. 1b), both Ce doping and PDMS modification increase the contact angle of PbO_2/SS electrode, which changes from hydrophilic to hydrophobic: Ce-PDMS/SS (98.4°, inset in Fig. 1e), PDMS-PbO_2/SS (108.3°, inset in Fig. 1h). For Ce-PDMS-PbO_2/SS, the contact angle is further increased to 110.6° (inset in Fig. 1k), and the surface hydrophobicity of the electrode is obviously improved. Previous studies [29,35] have shown that the hydrophobicity of PbO_2/SS electrode surface is beneficial to the release of hydroxyl radical in the catalytic process, thus improving the utilization rate of hydroxyl radical and its catalytic degradation efficiency of organic pollutants.
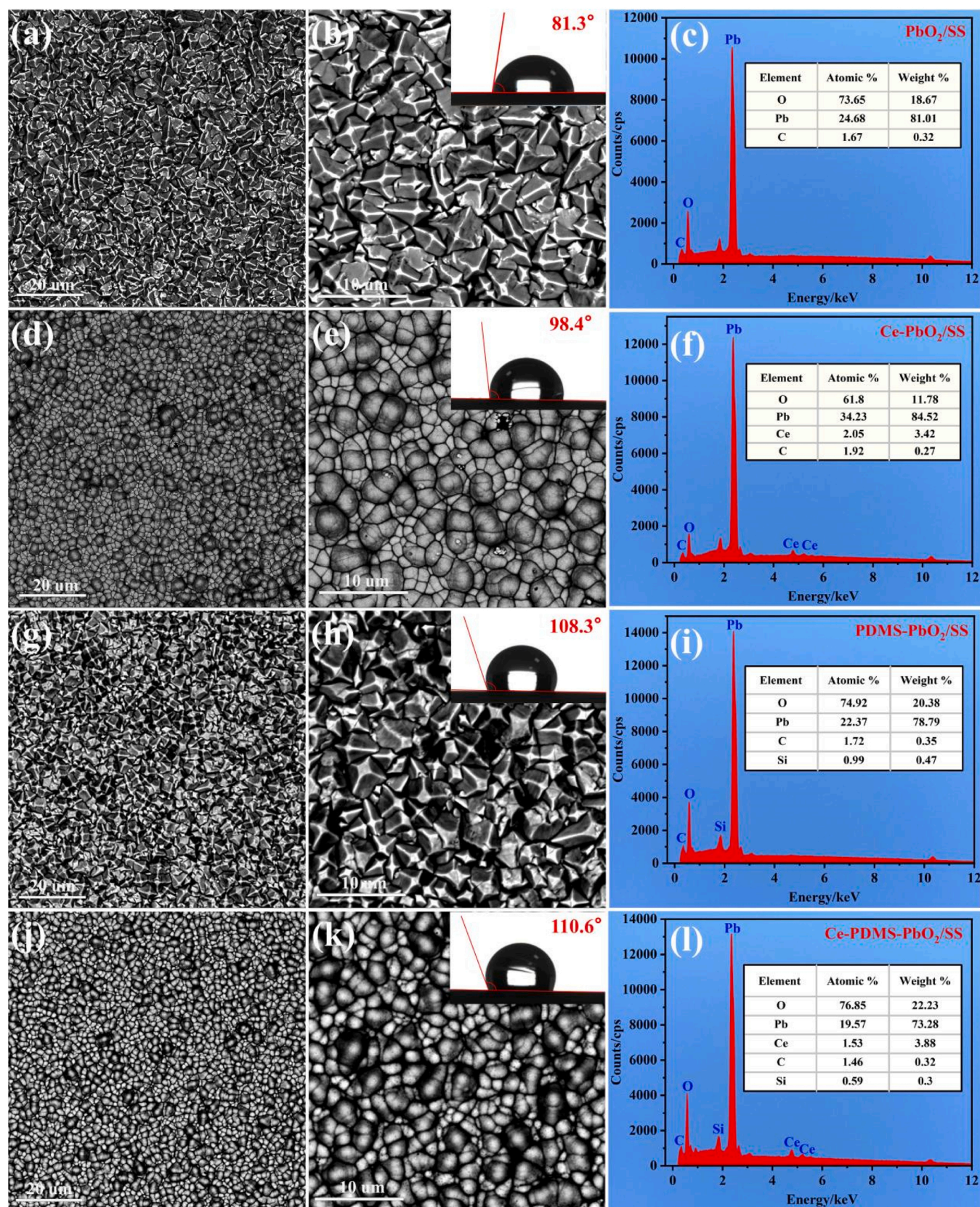
The elemental analysis of each PbO_2/SS electrode surface was carried out by energy dispersive spectrometer, and the results are shown in Fig. 1c-l. The surfaces of the four electrodes are mainly composed of O and Pb elements, and the active layer of Ce-PDMS-PbO_2/SS composite electrode is composed of five elements (O, Pb, C, Ce, and Si), and the contents of C, Si, and Ce are relatively low. From the EDS elemental mapping images, it can be seen that C, Pb, O, and Ce elements are homogeneously dispersed on Ce-PDMS-PbO_2/SS electrode surface (Fig. S6), while the weight percentage and atomic percentage of Ce element is 3.88 *wt*% and 1.53 *at*%, respectively (Fig. 1l). C and Si elements come from PDMS, while Ce comes from Ce^{3+}. The energy spectrum results confirm the successful doping of Ce and the surface modification of PDMS in the modified PbO_2/SS electrode.

Additionally, the TEM image of Ce-PDMS-PbO_2/SS in Fig. S7a demonstrates that the PbO_2 peeled off from the electrode surface exhibits sheet structure. While the HRTEM image clearly shows crystalline nature with lattice fringe spacing of 0.19, 0.28, and 0.35 nm (Fig. S7b), corresponding to the (211), (101), and (110) facets of β-PbO_2 phase consistent with the XRD spectrum below (Fig. 2a), respectively. The selected area electron diffraction (SAED) pattern of Ce-PDMS-PbO_2/SS illustrates clear diffraction spots (Fig. S7c), indicating the as-fabricated PbO_2 owns good crystallinity.
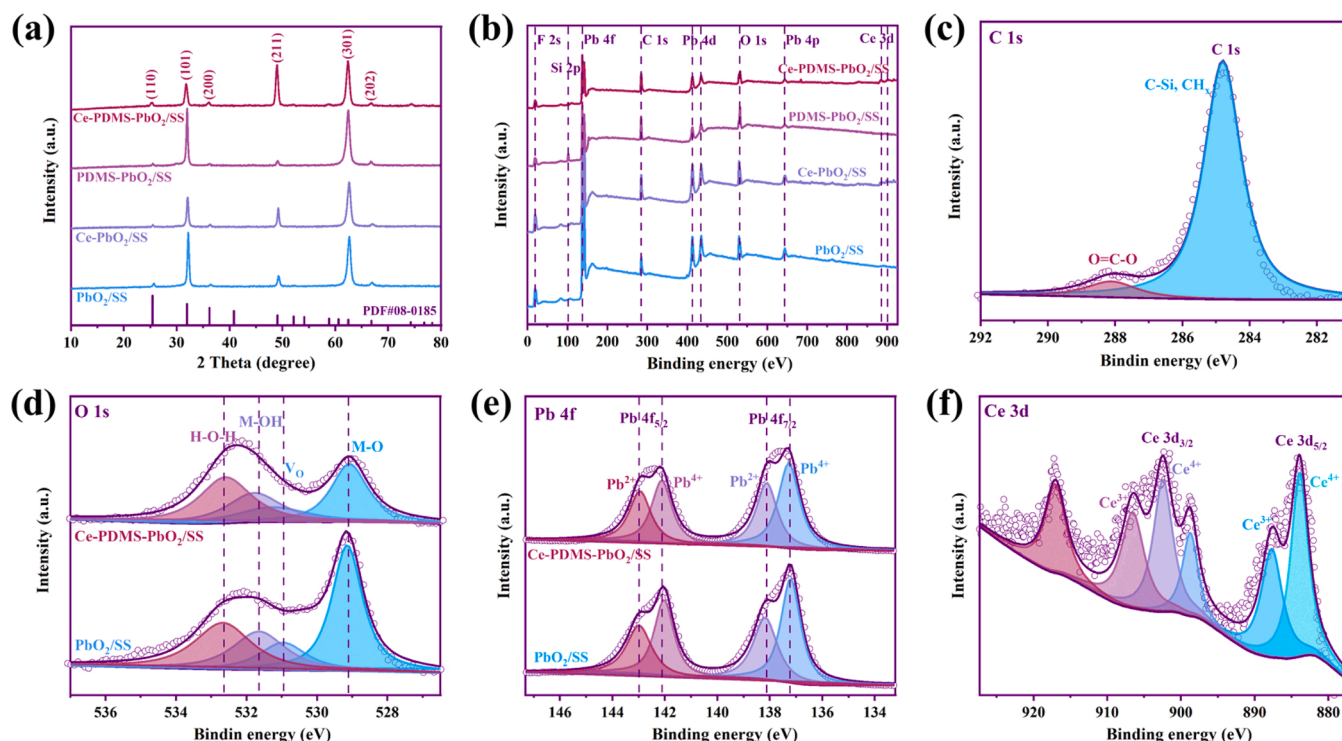
3.1.2. Electrode surface spectral analysis

The X-ray diffraction results of PbO_2/SS, Ce-PbO_2/SS, PDMS-PbO_2/SS, and Ce-PDMS-PbO_2/SS electrodes are shown in Fig. 2a, respectively. One can find that the XRD peak positions of the four electrodes are basically the same as the standard pattern of β-PbO_2 (PDF#08–0185), revealing the four kinds of PbO_2/SS electrodes are mainly β-PbO_2. The X-ray diffraction peaks of PbO_2 are principally located at $2\theta = 32.2°$, 36.2°, 49.2°and 62.6°, which belong to the β-PbO_2 crystal planes of (101), (200), (211), and (301), respectively. For two kinds of Ce-doped PbO_2 electrodes: Ce-PbO_2/SS and Ce-PDMS-PbO_2/SS composite electrodes, compared with pure PbO_2/SS electrodes, the crystal plane peak intensity changes obviously, that is, the (101) crystal plane peak decreases while the (211) crystal plane peak increases, which indicates that the doping of Ce impacts the preferred growth orientation of PbO_2 crystal plane, thus changing the apparent morphology and structure of PbO_2. Besides, the fine grain size and dense structure of Ce-PDMS-PbO_2/SS composite electrode are attributed to the doping of Ce element. In the process of electrodeposition, the Ce oxide particles deposited on the anode surface will reduce the active surface area of the substrate and hinder the crystallization of the surface of non-conductive particles, thus hindering the continuous growth of lead dioxide microcrystals. As we all know, smaller particle size can form larger active surface area beneficial to improving the electrocatalytic activity of electrodes. Therefore, the doping of Ce plays a positive role in promoting the catalytic activity of PbO_2/SS electrode for degradation. Moreover, the peak intensity of PDMS-PbO_2 crystal plane has no obvious change compared with PbO_2, suggesting that the surface modification of PDMS has little effect on the crystal structure of PbO_2.

In this study, XPS was also employed to characterize the element composition and the key element states of the electrode surface. Fig. 2b illustrates the XPS full spectrum of the four kinds of PbO_2 electrodes, showing the existence of O, Pb, F, and C elements, as well as the existence of Ce and Si in the modified electrodes, which are in agreement with the results of EDS analysis. Moreover, the chemical bonds and surface functional groups of the PbO_2 materials were analyzed via FT-IR (Fig. S8). All four PbO_2/SS electrodes show a typical Pb-O bond, that is, the characteristic bond at 1387.77 cm^{-1} [45]. And the two PbO_2/SS electrodes modified by PDMS exhibit a series of characteristic IR bands in the regions of 3000–2950 cm^{-1} (-CH_2 and -CH_3 stretching modes) and 1300–1000 cm^{-1} (Si-O-Si) [46]. FT-IR results reveal that PDMS was successfully modified on the surface of PbO_2. Fig. 2c-f illustrates the high-resolution XPS spectra of C 1s, O 1s, Pb 4f, and Ce 2p. Seen from the XPS peak fitting spectrum of C 1s (Fig. 2c) that there are C-Si bonds and CH_x with the binding energy of 284.8 eV on the electrode surface [47], and the O=C-O bond at 288.4 eV is formed by a small amount of oxidation of the C-H bond of PDMS in the PbO_2 electrodeposition process, the results show that PDMS can be adsorbed and deposited on the PbO_2 electrode surface. After fitting the XPS peak of O 1s in Fig. 2d, it is found that four different chemical states of oxygen exist in the PbO_2 coating, including crystal water (H-O-H), metal oxygen-hydrogen bond (M-OH, mainly Pb-OH), oxygen vacancy (V_O) and metal-oxygen bond (M-O, mainly Pb-O and Ce-O). The oxygen binding energies for these four chemical states are 532.8 eV, 531.7 eV, 530.9 eV, and 529.2 eV, respectively [45]. As shown in Fig. 3e, the Pb 4f pattern displays that the characteristic peaks of Pb $4f_{7/2}$ and Pb $4f_{5/2}$ appear in pairs, and the split-peak fitting spectra of Pb 4f indicate that the non-stoichiometric

Fig. 1. SEM images and EDS spectra of the PbO₂/SS anodes: (a-c) PbO$_2$/SS, (d-f) Ce-PbO$_2$/SS, (g-i) PDMS-PbO$_2$/SS, (j-l) Ce-PDMS-PbO$_2$/SS. Insets in b, e, h, and k are the associated water contact angles.

Fig. 2. XRD diffraction pattern (a) and XPS full spectrum pattern (b) of PbO$_2$/SS, Ce-PbO$_2$/SS, PDMS-PbO$_2$/SS and Ce-PDMS-PbO$_2$/SS electrodes; (c) C 1s spectra of Ce-PDMS-PbO$_2$/SS electrode, O 1s (d) and Pb 4f (e) spectra of PbO$_2$ and Ce-PDMS-PbO$_2$ electrodes; (d) Ce 3d spectra of Ce-PDMS-PbO$_2$ electrode.

PbO$_2$ contains Pb^{2+} and Pb^{4+} [48]. The binding energies at 138.1 and 143.0 eV are credited to PbO, while the peaks of PbO$_2$ are located at 137.3 and 142.2 eV [49]. According to the binding energies of Ce 3d$_{3/2}$ (916.9 and 898.4 eV) and Ce 3d$_{5/2}$ (901.1 and 882.4 eV) and other binding energies (885.5 and 906.1 eV), it can be confirmed that two valence states Ce^{4+} and Ce^{3+} exist in the sample [27]. Therefore, the doped Ce mainly exists in the form of CeO$_2$ and Ce$_2$O$_3$, which are coated in PbO$_2$ grains. And the relative ratio of CeO$_2$ and Ce$_2$O$_3$ is 53.6% and 46.4% calculated from the fitting data. Furthermore, the fitting calculation results show that after Ce doping, the Vo content increases from 13.31% to 15.14%, and the M-OH content increases from 20.41% to 22.28%, which is beneficial to improving the catalytic performance of PbO$_2$/SS electrode. The spectral analysis results reveal that Ce^{3+} and PDMS have successfully modified the PbO$_2$/SS electrode surface, the surface crystal structure of PbO$_2$ and the electronic environment of the central metal lead have changed significantly.

3.2. Electrochemical performance analysis of the electrodes

3.2.1. Oxygen evolution potential and exchange current density (LSV)

Electrochemical characterization-LSV was employed to detect the oxygen evolution potential (*OEP*) and catalytic reaction rate of different electrodes. As seen from Fig. 3a and Table 1 that the *OEP* of Ce-PDMS-PbO$_2$/SS electrode demonstrates the lowest value of 1.55 V, indicating the modified PbO$_2$/SS electrode possesses higher electrocatalytic activity and the catalytic reaction could be carried out more easily on the electrode surface. Numerous literature have shown that the Tafel slope *b* can be applied to compare the catalytic efficiency of oxygen evolution at the electrode [50,51]. And the Tafel linear fitting curves from the stable LSV oxygen evolution zone for various PbO$_2$ electrodes are illustrated in Fig. 3b, the kinetic parameters were calculated using Eq. 1 [52]:
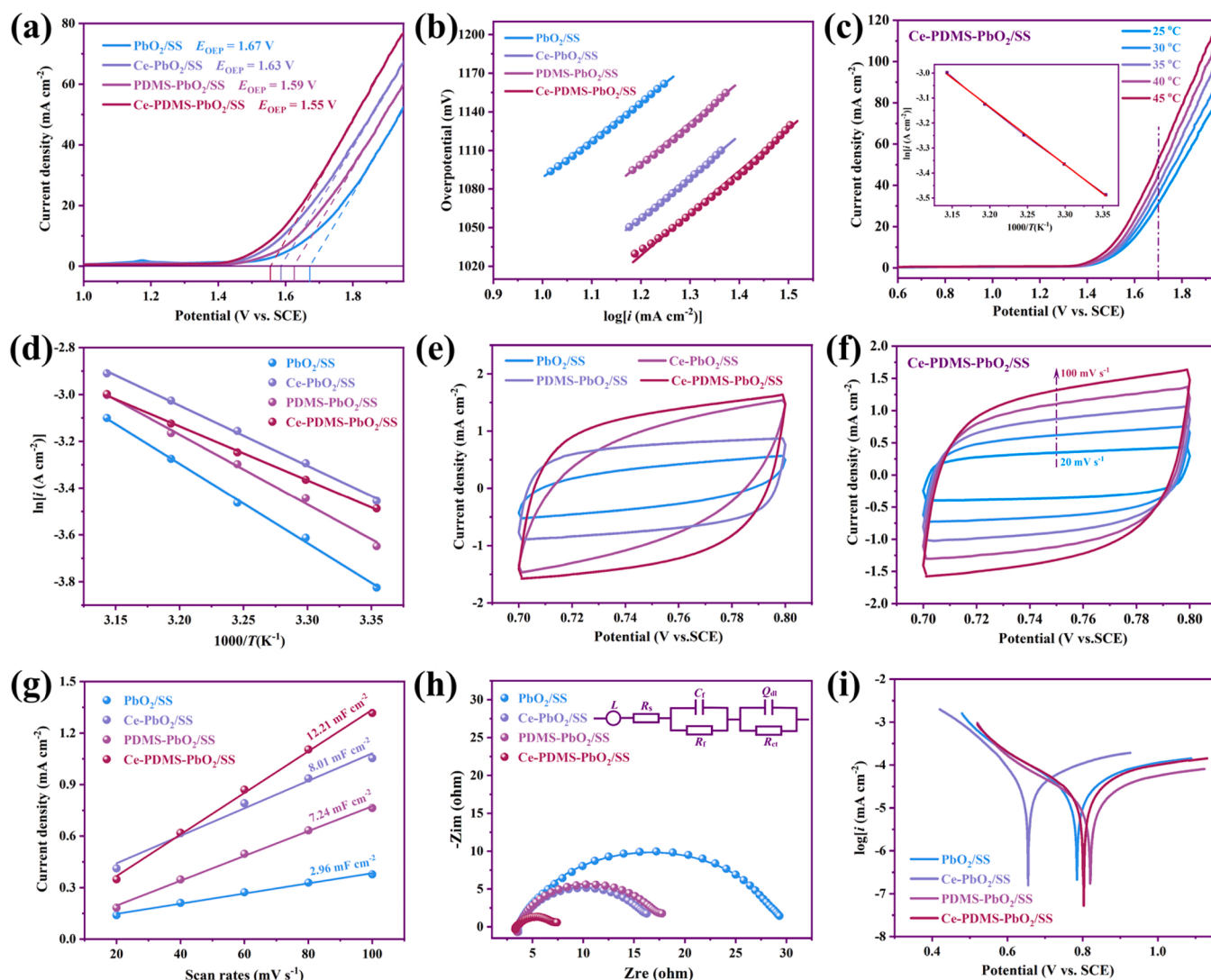
$$\eta = a + b\log i \tag{1}$$

where η is the oxygen evolution overpotential, and i is the faradaic current density. It is obvious that Ce-PDMS-PbO$_2$/SS displays the highest

Tafel slope (328.4 mV dec^{-1}), indicating its lower electrocatalytic efficiency for oxygen evolution. Generally, the higher exchange current density (j^0) indicates that the electrode reaction rate is faster, and the electrons are mainly applied for the consumption of electrocatalytic reaction, not for increasing the electrode polarization [53]. From the fitting calculation results, the Ce-PDMS-PbO$_2$/SS electrode exhibits the highest j^0 value of 1.171 × 10^{-5} A cm^{-2} about 1–5 times higher than the above three electrodes, showing the best electrocatalytic activity. This result reveals that the catalytic reaction is more likely to take place on the surface of the modified electrode, and the driving force required for the reaction decreases and the possibility increases with the reaction going on. Obviously, the doping of Ce and the surface modification of PDMS can promote the surface catalytic reaction occurrence of the PbO$_2$/SS electrode and significantly enhance the electrocatalytic activity.

3.2.2. Activation energy analysis (E_a)

By comparing the activation energy values of the four PbO$_2$/SS electrodes, the electrocatalytic activity can be studied [54,55]. Based on Arrhenius law, the activation energy can be determined by employing Eq. S1. And Fig. 3c displays the LSV curves of Ce-PDMS-PbO$_2$/SS electrode in 0.5 M Na$_2$SO$_4$ solution at different temperatures and the relevant ln*i*-1/*T* linear fitting curve, while, the corresponding measurement curves of PbO$_2$/SS, Ce-PbO$_2$/SS, and PDMS-PbO$_2$/SS electrodes are illustrated in Fig. S9a-c. One can find that the current densities of four electrodes increase with the increase of temperature at a certain potential, indicating that temperature can accelerate the catalytic reaction rate. The fitting curves of ln*i*-1/*T* for the four PbO$_2$/SS electrodes are illustrated in Fig. 3d, and the corresponding activation energy fitting results are exhibited in Table 2. It can be obviously found that the Ce-PDMS-PbO$_2$/SS composite electrode exhibits the lowest E_a value of 19.20 kJ mol^{-1} in contrast to the other three PbO$_2$/SS electrodes. The lower the energy barrier of electrocatalytic water oxidation is, the easier the conversion of water to reactive oxygen species (ROS) is, and the stronger the electrocatalytic activity is. Consequently, the above results

Fig. 3. Electrochemical measurements of the four PbO_2 electrodes in 0.5 M Na_2SO_4 electrolyte at 25 ℃, including (a) LSV curves; (b) Tafel linear fitting curves; (c) LSV curves of Ce-PDMS-PbO_2/SS electrode at various temperatures; (d) ln$i$-1/T fitting curves; (e) narrow potential CV curves; (f) narrow potential CV curves of Ce-PDMS-PbO_2/SS electrode at various scan rates. (g) C_{dl} linear fitting curves; (h) EIS spectrum diagram and corresponding equivalent circuit diagram; (i) Tafel curves.

Table 1

Kinetic parameters of polarization curve fitting for PbO_2/SS, Ce-PbO_2/SS, PDMS-PbO_2/SS, and Ce-PDMS-PbO_2/SS electrodes.

	PbO_2/SS	Ce-PbO_2/SS	PDMS-PbO_2/SS	Ce-PDMS-PbO_2/SS
a (mV)	793.6	674.8	720.5	634.3
b (mV dec^{-1})	295.2	319.2	316.2	328.4
j^0 (A cm^{-2})	2.048×10^{-6}	7.688×10^{-6}	5.264×10^{-6}	1.171×10^{-5}
OEP (V)	1.67	1.59	1.63	1.55

Table 2

Activation energy E_a, double layer capacitance C_{dl} and $ECSA$ fitting values of PbO_2/SS, Ce-PbO_2/SS, PDMS-PbO_2/SS, and Ce-PDMS-PbO_2/SS electrodes.

	PbO_2/SS	Ce-PbO_2/SS	PDMS-PbO_2/SS	Ce-PDMS-PbO_2/SS
E_a (kJ mol^{-1})	28.19	21.41	24.78	19.20
C_{dl} (mF cm^{-2})	2.96	8.01	7.24	12.12
$ECSA$ (cm^2)	49.3	133.5	120.7	202.0

reveal that the doping of Ce and the modification of PDMS can promote the formation of ROS on the electrode surface, thus promoting the occurrence of catalytic reaction. The results are in agreement with the above electrochemical and physical characterization results.

3.2.3. Electrochemical active surface area (ECSA)

The double layer capacitance (C_{dl}) and electrochemical active area of the four PbO_2/SS electrodes were measured by cyclic voltammetry to explore the effects of Ce doping and PDMS modification on the surface layer of PbO_2. From the CV curves of different PbO_2/SS anodes (Fig. 3e), it can be observed that under the potential interval of 0.7–0.8 V, the CV curve of the unmodified PbO_2/SS anode has the smallest capacitance, while the capacitance of the modified Ce-PbO_2/SS, PDMS-PbO_2/SS, and Ce-PDMS-PbO_2/SS anodes have increased in varying degrees, among which the CV curve of Ce-PDMS-PbO_2/SS anode has the largest CV integral area, that is, the maximum voltammetric charge, indicating it possesses more catalytic active centers [22]. Additionally, the electrochemical active area is related to the number of electroactive centers, which can reflect the electrocatalytic activity of the electrode [49,56]. Fig. 3f shows the CV curves of Ce-PDMS-PbO_2/SS anode at various scan rates in the double-layer capacitance range (0.7–0.8 V), and the corresponding CV curves of PbO_2/SS, Ce-PbO_2/SS, and PDMS-PbO_2/SS

electrodes are shown in Fig. S10a-c. The fitting curves of i_E (the positive current density at 0.75 V) versus v (scan rate) and the corresponding C_{dl} values are demonstrated in Fig. 3g and Table 2, respectively. Hence, the *ECSA* values of the electrodes are estimated by Eq. 2:

$$ECSA = \frac{C_{dl}}{C_S} \times S \tag{2}$$

where C_S is the specific capacitance and S is the electrode surface area [57]. Based on the previous literature, the C_S value is 60 μF cm^{-2} [45, 58], thus the *ECSA* values are obtained. Compared with PbO$_2$/SS (49.3 cm^2), the *ECSA* value of Ce-PbO$_2$/SS and PDMS-PbO$_2$/SS increased significantly to 133.5 and 120.7 cm^2, respectively, while the *ECSA* value of Ce-PDMS-PbO$_2$/SS further increased to 202.0 cm^2, exhibiting a higher active surface area. Therefore, the co-modification of Ce and PDMS can significantly improve the *ECSA* on the PbO$_2$/SS electrode surface, which is beneficial to the improvement of electrocatalytic activity.

3.2.4. Electrochemical impedance spectroscopy (EIS)

To further explore the charge transfer rate and the electrochemical reaction mechanism of the PbO$_2$ electrodes, EIS measurement was performed at 1.55 V. Fig. 3h illustrates the experimental and fitted EIS spectra of PbO$_2$/SS, Ce-PbO$_2$/SS, PDMS-PbO$_2$/SS and Ce-PDMS-PbO$_2$/SS electrodes. To explain the EIS spectrum, the equivalent circuit $LR_s(R_fC_f)(Q_{dl}R_{ct})$ shown in Fig. 3h is employed to fit and model the impedance behavior of the electrodes [52], and the fitting parameters for the EIS data are listed in Table 3. The Nyquist curves of all electrodes are similar in form, which is characterized by an inductance arc L and solution resistance R_s in the high-frequency region. While it can be clearly seen from the Bode plots for the four electrodes (Fig. S11) that there appear two peaks in each PbO$_2$ electrode, demonstrating there exist two continuous (RC) loops in the EIS spectrum (Fig. 3h), that is, a capacitor-resistance arc and a sunken capacitance-resistance arc. In the model, the inductance L in the high-frequency region is caused by the shielding effect [53], the semicircular capacitive reactance arc (R_fC_f) in the middle-frequency region is related to the physical response of the pore structure on the electrode surface, while the low-frequency sunken semicircular capacitive arc shows a normal phase element (*CPE*) and charge transfer resistance (R_{ct}) in the equivalent circuit, which represents the electrochemical discharge process, and its behavior reflects the electrochemical performance of the electrode [59]. Previous studies have shown that larger Q_{dl} and smaller R_{ct} values are considered more conducive to the catalytic reactions occurrence [60,61]. And the Ce-PDMS-PbO$_2$/SS electrode displays a small sunken impedance arc, showing a good ability for electron transfer. As shown in Table 3, the R_{ct} value of Ce-PDMS-PbO$_2$/SS is as low as 3.268 Ω, which is only 1/8 that of PbO$_2$/SS, 4/9 that of Ce-PbO$_2$/SS and 3/7 that of PDMS-PbO$_2$/SS, respectively. Moreover, the Q_{dl} value of Ce-PDMS-PbO$_2$/SS electrode also demonstrates a maximum value of 4.545×10^{-2} S·s^n·cm^{-2} nearly two orders of magnitude higher than that of PbO$_2$/SS. These results indicate that the doping of Ce and the surface modification of PDMS can improve the electrochemical behavior of the electrode and promote the electrocatalytic reaction process.

3.2.5. Corrosion resistance analysis (Tafel)

As one of the key parameters for practical application, corrosion resistance of the four PbO$_2$/SS electrodes was performed by using Tafel measurement in 0.5 M Na$_2$SO$_4$ solution exhibited in Fig. 3i. As listed in Table 4, the corrosion current density of Ce-doped PbO$_2$/SS electrode is higher than that of the unmodified electrode, demonstrating that Ce doping will reduce the electrode corrosion resistance. Among the three modified electrodes, the PDMS-modified PbO$_2$ electrode not only exhibits the highest corrosion potential (0.821 V) but also possesses the lowest corrosion current density (16.16 μA cm^{-2}), showing its outstanding corrosion resistance. Furthermore, the PbO$_2$ electrode co-modified with Ce and PDMS illustrates lower corrosion current density and larger Tafel slope, indicating its excellent corrosion resistance.
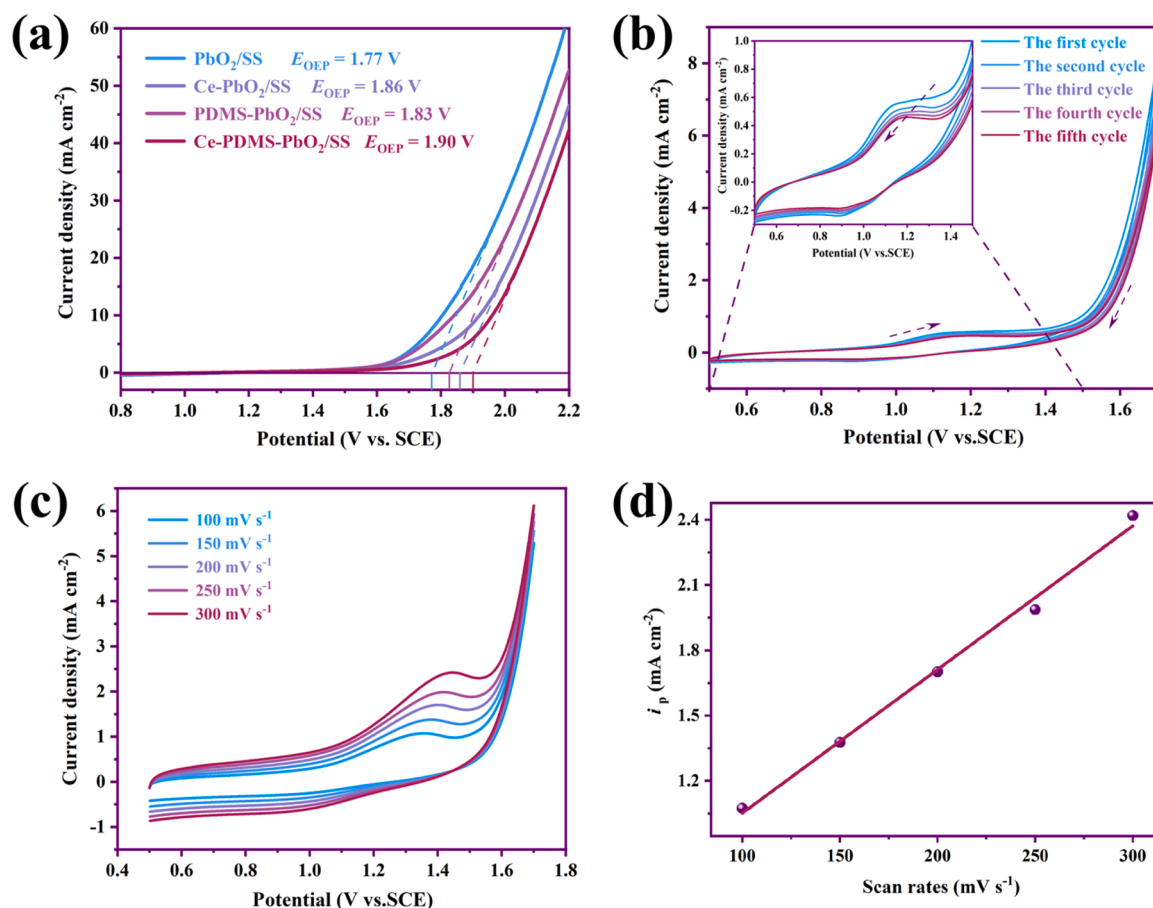
3.3. Electrochemical degradation of PNP

3.3.1. Electrochemical analysis

Fig. 4a shows the LSV curves obtained with different PbO$_2$/SS electrodes at the scan rate of 5 mV s^{-1} in 0.5 M Na$_2$SO$_4$ electrolyte containing 500 mg L^{-1} PNP. In 0.5 M Na$_2$SO$_4$ solution, compared with the solution without PNP, the *OEP* value of the electrodes in the solution containing PNP increased obviously. Significantly, the *OEP* value of Ce-PDMS-PbO$_2$/SS electrode shows the most remarkable increase (Fig. S12), owing to large amounts of ·OH were employed for PNP degradation inhibited the competitive oxygen evolution reaction during the anodic oxidation reaction [62], demonstrating the catalytic degradation ability of this electrode to PNP is higher than that of the other three electrodes.

To further investigate the electrocatalytic degradation of PNP at the composite electrode, the adsorption behavior of PNP on Ce-PDMS-PbO$_2$/SS electrode was performed applying continuous cyclic voltammetry, as illustrated in Fig. 4b. And a pair of obvious redox peaks can be seen in the first scan. The potential and current density of the oxidation peak is 1.164 V and 5.606×10^{-4} A cm^{-2}, respectively. This peak potential position is basically in agreement with that characterized in the previous literature [63], corresponding to the PNP oxidation peak. In the oxidative degradation process, the catalytic reaction will consume numerous hydroxyl radicals adsorbed on the electrode surface. With the strong oxidation peak appearing, between the active layer on the electrode surface and PNP, there occurs a process with direct electron transfer. The results indicate that PNP is mainly degraded by the oxidation of physically adsorbed hydroxyl radicals and chemisorbed

Table 4

Tafel polarization parameters of PbO$_2$/SS, Ce-PbO$_2$/SS, PDMS-PbO$_2$/SS, and Ce-PDMS-PbO$_2$/SS electrodes in 0.5 M Na$_2$SO$_2$ electrolyte solution.

Sample	E_{corr} (V vs. SCE)	j_{corr} (μA cm^{-2})	β_c (mV dec^{-1})	β_a (mV dec^{-1})
PbO$_2$/SS	0.785	26.19	169.1	214.5
Ce-PbO$_2$/SS	0.655	35.83	111.7	225.4
PDMS-PbO$_2$/SS	0.821	16.16	183.3	219.8
Ce-PDMS-PbO$_2$/SS	0.803	21.36	175.5	211.6

Table 3

EIS equivalent circuit fitting parameters for the four PbO$_2$ electrodes.

	PbO$_2$/SS	Ce-PbO$_2$/SS	PDMS-PbO$_2$/SS	Ce-PDMS-PbO$_2$/SS
L (H cm^{-2})	5.716×10^{-7}	1.323×10^{-6}	1.361×10^{-6}	6.159×10^{-7}
R_s (Ω cm^{-2})	3.428	3.524	3.436	3.302
C_f (F cm^{-2})	9.371×10^{-5}	3.052×10^{-3}	2.784×10^{-3}	2.089×10^{-3}
R_f (Ω cm^{-2})	0.2106	6.454	7.896	1.603
Q_{dl} (S·s^n·cm^{-2})	4.696×10^{-4}	1.597×10^{-2}	2.417×10^{-2}	4.545×10^{-2}
n	0.8275	0.6443	0.5822	0.4654
R_{ct} (Ω cm^{-2})	25.93	7.391	7.738	3.268
x^2	2.091×10^{-4}	3.251×10^{-5}	6.212×10^{-5}	9.366×10^{-5}

Fig. 4. (a) LSV curves of the four PbO$_2$/SS electrodes in 0.5 M Na$_2$SO$_4$ electrolyte containing 500 mg L^{-1} PNP; (b) continuous CV curves of Ce-PDMS-PbO$_2$/SS electrode in 0.5 M Na$_2$SO$_4$ electrolyte containing 500 mg L^{-1} PNP; (c) CV curve of Ce-PDMS-PbO$_2$/SS electrode at various scan rates in electrolyte and (d) linear fitting curve of CV scan rates versus peak current density.

PbO$_{2+x}$ compounds [53]. With the increase of cyclic voltammetry scanning times, the PNP degradation peak potential continues to negative shift, suggesting that other intermediates after PNP degradation are also adsorbed on the electrode surface, affecting the degradation process of PNP. Moreover, the oxidation peak current density of PNP gradually decreases to 4.588 × 10^{-4} A cm^{-2}. This is owing to that the PNP adsorbed on the electrode surface is degraded into other intermediates covering some active sites after the first CV cycle, which prevents the further oxidation of PNP and reduces the degradation efficiency. However, the electrode passivation is not obvious in the process of PNP electrocatalytic degradation, and the surface of electrode is still capable of high catalytic degradation ability.

In order to investigate which type of process controls the PNP degradation, CV curves with various scan rates (100–300 mV s^{-1}) were employed to detect in this work, as illustrated in Fig. 4c-d. As seen from Fig. 4c that the oxidation peak potential shifts positively and the corresponding peak current density enhances with the scan rate increase. Taking the scan rate (v) as the abscissa and the peak current density (I_p) at different scan rates as the ordinate, Fig. 4d is obtained by linear fitting. And the fitting results demonstrate there exists a nice linear relationship between the scan rates and the peak current densities, implying that the adsorption process of PNP controls the PNP degradation [64].

3.3.2. Comparison of hydroxyl radical production

Electron paramagnetic resonance (EPR, Bruker EMXPLUS) was applied to reveal the reactive radicals generated with Ce-PDMS-PbO$_2$/SS anode in the electrochemical system. 5,5-Dimethyl-1-pyrroline-N-oxide (DMPO) was employed as a spin-trapping agent to trap possible free radicals of ·OH, superoxide (·O$_2^-$), and sulfate (·SO$_4^-$). As illustrated in Fig. 5a, the typical DMPO-·OH signal peaks with an intensity ratio of 1:2:2:1 are exhibited in EPR spectra[65]; while the signals of DMPO-·O$_2^-$ and DMPO-·SO$_4^-$ detected in electrolysis solution are weak, demonstrating that ·OH are the predominant radical species in the electrochemical oxidation system [59]. Moreover, the EPR spectra of DMPO-·OH for the four PbO$_2$/SS electrodes were also obtained, as shown in Fig. 5b, the DMPO-·OH peaks intensity for PbO$_2$/SS are weak, while the intensity for Ce-PbO$_2$/SS and PDMS-PbO$_2$/SS is stronger, and the strongest intensity for Ce-PDMS-PbO$_2$/SS, indicating that Ce doping and PDMS modification can enhance the ·OH generation ability of the PbO$_2$/SS electrodes and the Ce-PDMS-PbO$_2$/SS electrode possesses the highest ability for ·OH generation in the electrochemical system[66].

Furthermore, the fluorescence spectroscopic technique [67] was also employed to determine the hydroxyl radical production ability of PbO$_2$/SS, Ce-PbO$_2$/SS, PDMS-PbO$_2$/SS, and Ce-PDMS-PbO$_2$/SS electrodes. Fig. S13a-d shows the fluorescence spectra of PbO$_2$/SS, Ce-PbO$_2$/SS, PDMS-PbO$_2$/SS, and Ce-PDMS-PbO$_2$/SS electrodes observed. And the fluorescence signals of all electrodes appear at 425 nm, demonstrating that all electrodes can generate ·OH free radicals. Comparing the fluorescence intensity of different electrodes at various reaction times, the fluorescence intensity of PbO$_2$/SS electrode is the weakest, while obviously stronger for those of Ce-PbO$_2$/SS and PDMS-PbO$_2$/SS electrodes, and the strongest for Ce-PDMS-PbO$_2$/SS electrode. For instance, the fluorescence intensity of Ce-PDMS-PbO$_2$/SS is 905.2 after the whole electrolysis process, while those of PbO$_2$/SS, Ce-PbO$_2$/SS, and PDMS-PbO$_2$/SS are 540.1, 795.0, and 811.1, respectively. Hence, the cumulative concentration value of ·OH on the modified electrodes Ce-PbO$_2$/SS, PDMS-PbO$_2$/SS, and Ce-PDMS-PbO$_2$/SS at
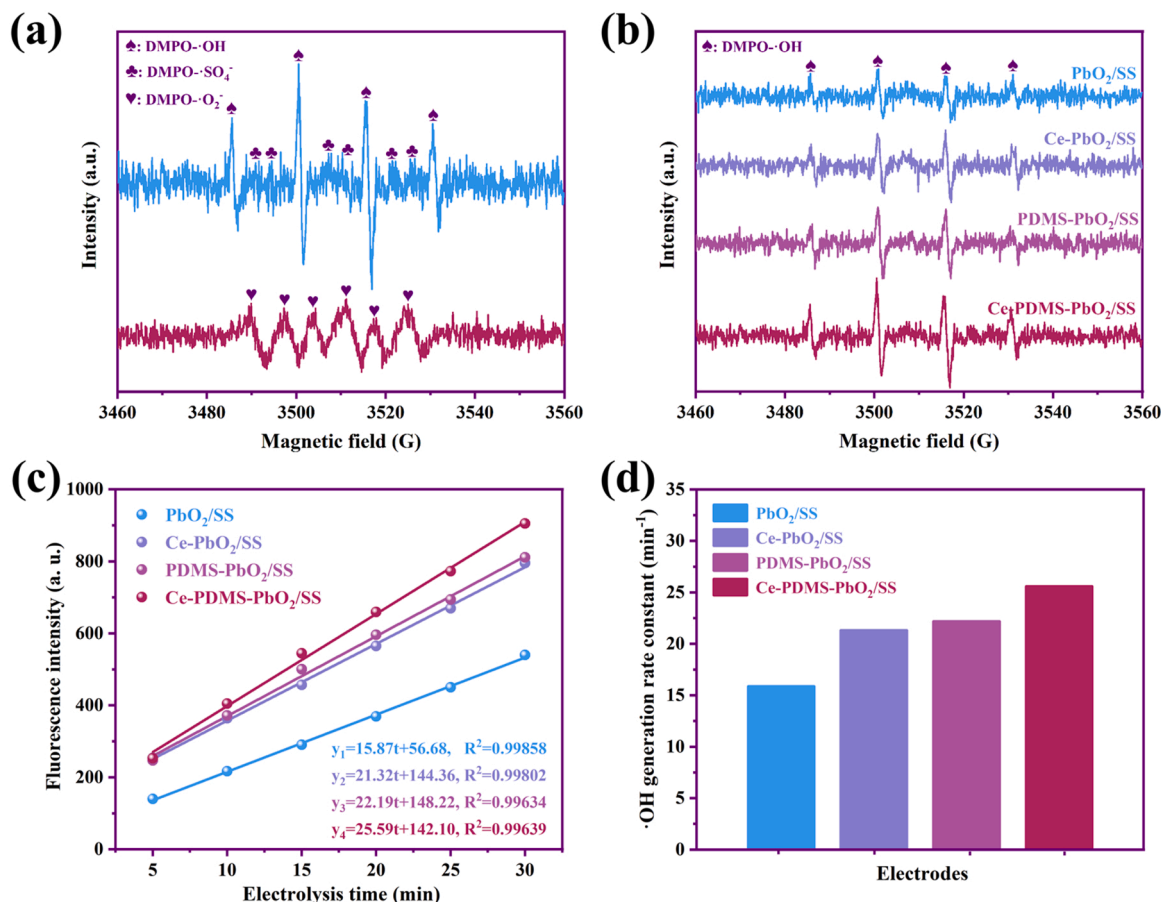
Fig. 5. (a) EPR spectra of the free radicals in the electrochemical oxidation system with Ce-PDMS-PbO$_2$/SS; (b) DMPO trapped EPR spectrometry for PbO$_2$/SS, Ce-PbO$_2$/SS, PDMS-PbO$_2$/SS and Ce-PDMS-PbO$_2$/SS; (c) fitting diagram of fluorescence intensity versus reaction time of 2-hydroxyterephthalic acid with different PbO$_2$/SS electrodes as anodes; (d) histogram of ·OH free radical generation rate of different PbO$_2$/SS electrodes.

the end of the whole electrolysis process are 1.47, 1.50, and 1.68 times that of the PbO$_2$/SS electrode, respectively. Furthermore, one can observe that the fluorescence intensity of each electrode enhanced linearly with the prolongation of the reaction time. As demonstrated in Fig. 5c-d, if the concentration of ·OH is represented by fluorescence intensity, there exists a good linear relationship between d[·OH]/dt and t, indicating that the ·OH formation of all electrodes follows the quasi-zero order reaction [63], the order of the generation rate constant k (the fitting line slope of fluorescence intensity versus t) is as follows: Ce-PDMS-PbO$_2$/SS>PDMS-PbO$_2$/SS>Ce-PbO$_2$/SS>PbO$_2$/SS. These results illustrate that the doping of Ce and the surface modification of PDMS enhance the ability of PbO$_2$/SS electrode to produce ·OH radical, owing to the co-modification could provide more catalytic active sites for the coating of PbO$_2$/SS electrode.

3.3.3. Degradation Kinetics and removal efficiency of PNP

PNP solutions with concentrations of 0.5, 1.0, 2.0, 4.0, 6.0, 8.0, and 10.0 mg L^{-1} were prepared, and dilute nitric acid solution was applied to regulate the pH of PNP solution. Then the relationship between absorbance and PNP concentration was determined by UV–vis spectrophotometer, and the standard curve was obtained by the corresponding data of absorbance concentration. The relevant measurement curves and absorbance-concentration standard curve of pH = 3 are shown in Fig. S14a-b. Adopt Eq. 3 :

$$\eta_{RE} = \frac{C_0 - C_t}{C_0} \times 100\% \tag{3}$$

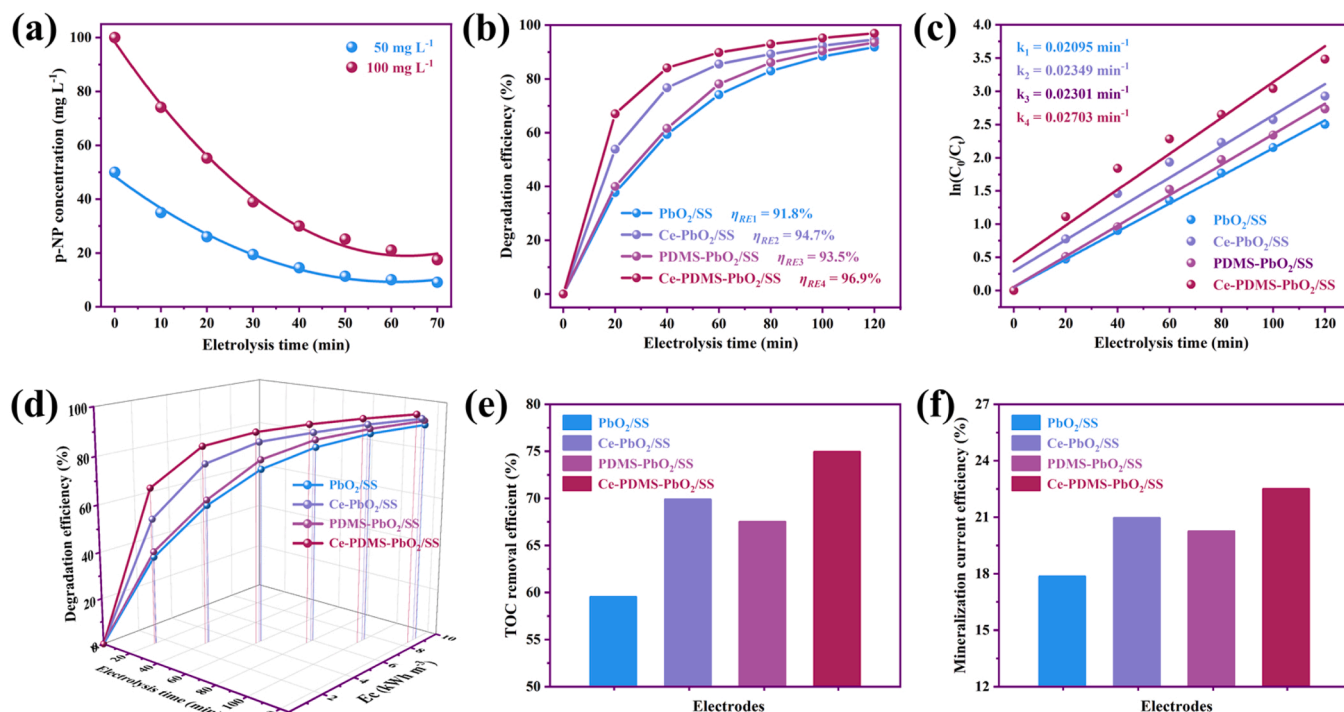to calculate the degradation efficiency of PNP. The effect of conditions

on PNP degradation efficiency were also explored and analyzed, as shown in Fig. S15 and Content S1.

The reaction order of PNP degradation by Ce-PDMS-PbO$_2$/SS electrode was studied via the half-life method in this work. By degrading PNP with various initial concentrations of 50 and 100 mg L^{-1}, the curves for the relationship between the degradation time and the PNP concentration were obtained. Fig. 6a shows the polynomial fitting relationship between different initial PNP concentrations and degradation time. When the PNP concentration is degraded to half of the initial, the corresponding time is considered as the half-life $t_{1/2}$. While the half-life time is obtained through the fitting curves: $t_{1/2} = 23.75$ min, $t'_{1/2} = 22.01$ min, and then replace it into Eq. 4 [53]:

$$n = 1 + \frac{\lg(t_{1/2}/t'_{1/2})}{\lg(c'_0/c_0)} \tag{4}$$

the reaction order is calculated to be $n = 0.9123$. Consequently, the electrocatalytic oxidation of PNP with Ce-PDMS-PbO$_2$/SS electrode belongs to a quasi-first-order reaction, according to the kinetic law of quasi-first-order reaction.

To further evaluate the degradation ability of PNP by various electrodes, the four PbO$_2$/SS electrodes were employed as anodes to degrade PNP. And the degradation efficiency and kinetic fitting curves of PNP for the four PbO$_2$/SS electrodes are demonstrated in Fig. 6b-c. Fig. 6b shows that the PNP removal efficiency increases with the increase of degradation time. After 120 min electrolysis time, the PNP degradation efficiency of Ce-PDMS-PbO$_2$/SS electrode is 96.9%, while those of PbO$_2$/SS, Ce-PbO$_2$/SS, and PDMS-PbO$_2$/SS electrodes are 91.8%, 94.6%, and 93.5%, respectively. Additionally, the linear relationship between ln
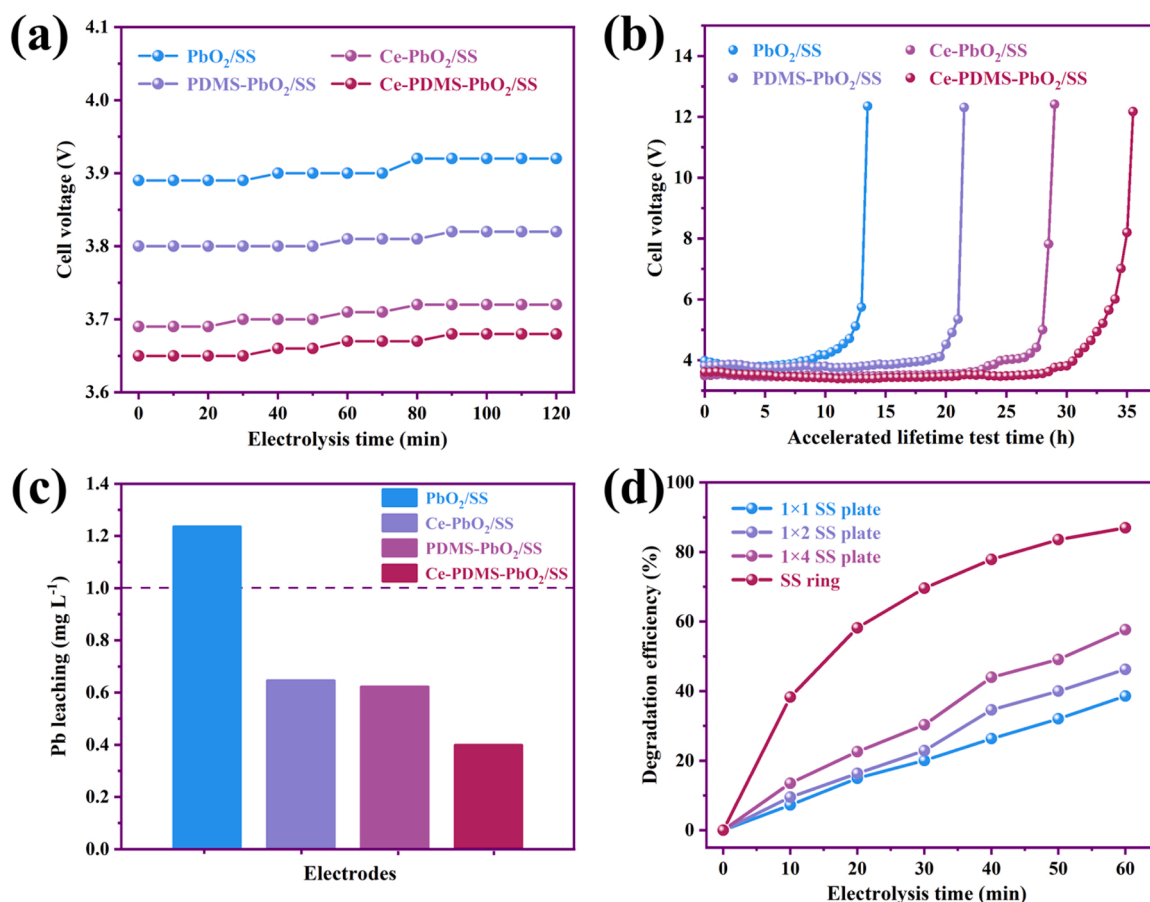
Fig. 6. (a) Polynomial fitting curves of Ce-PDMS-PbO$_2$/SS electrode in 0.5 M Na$_2$SO$_4$ solution with 50 and 100 mg L^{-1} PNP; (b) PNP degradation efficiency-time curves, (c) degradation kinetics linear fitting curves, (d) degradation efficiency, energy consumption-time curves, (e) TOC removal efficiency histogram and (f) PNP mineralization efficiency histogram of the four PbO$_2$/SS electrodes in 120 min degradation time.

(C_0/C_t) and electrolysis time is displayed in Fig. 6c, demonstrating the degradation process conforms to quasi-first-order reaction kinetics. And the kinetic constants of degradation reaction at different electrodes were calculated to be 0.02095, 0.02349, 0.02301, and 0.02703 min^{-1}, respectively. Moreover, the PNP degradation efficiency and kinetics constants of the four PbO$_2$/SS electrodes at various electrolysis time (60–120 min) are also summarized in Table S2, showing the superiority of Ce-PDMS-PbO$_2$/SS electrode for PNP degradation, especially at 60 min (Fig. S16). Besides, compared to the recently modified PbO$_2$ electrodes for the degradation of phenol or nitrobenzene pollutants, Ce-PDMS-PbO$_2$/SS electrode also displays outstanding catalytic degradation ability with higher degradation kinetic constant at the lowest applying area (Table S3). All these results demonstrate that Ce-PDMS-PbO$_2$/SS electrode exhibits remarkable electrocatalytic activity and can degrade PNP more rapidly and effectively. The efficient degradation of PNP by Ce-PDMS-PbO$_2$/SS electrode can be attributed to two aspects: firstly, the doping of Ce optimizes the electronic environment of the Pb site in active center, changes the structure and morphology of PbO$_2$ and reduces the PbO$_2$ particle size, improves the conductivity and active area of the electrode, and provides more active sites for electron transfer and hydroxyl radical production; secondly, the surface modification of PDMS makes the surface of PbO$_2$/SS hydrophobic, which is beneficial to improving the generation rate and utilization rate of ·OH. The synergism of the two effects improves the degradation efficiency of PNP using Ce-PDMS-PbO$_2$/SS electrode. Additionally, the energy consumption of PNP degradation by different PbO$_2$/SS electrodes was calculated according to Eq. S2, as shown in Fig. 6d, the Ce-PDMS-PbO$_2$/SS electrode exhibits the fastest degradation rate of PNP and the lowest energy consumption. To further verify the mineralization effect of PNP, TOC tests were carried out on the electrolytes of the four electrodes before and after 120 min of PNP degradation. According to Eq. S3 and S4, the TOC removal and mineralization efficiency of these electrodes were calculated respectively, and the results are illustrated in Fig. 6e-f. The removal efficiency of TOC by Ce-PDMS-PbO$_2$/SS electrode is 74.9% higher than that of PbO$_2$/SS electrode (59.5%), Ce-PbO$_2$/SS (69.9%) and PDMS-PbO$_2$/SS

(67.5%), and also exhibits the highest mineralization efficiency (22.5%). This is owing to that the Ce-PDMS-PbO$_2$/SS electrode has a large specific surface area of electrocatalytic activity and a faster generation rate of hydroxyl radicals, synergistically promoting the degradation of PNP, decomposes it into small molecular acids and mineralizes them into water and carbon dioxide.
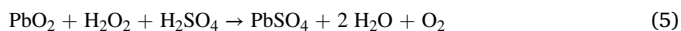
3.3.4. Stability of electrodes

To examine the stability of the four various PbO$_2$/SS electrodes, the variation trend of cell voltage with electrolysis time during degradation was recorded, and the accelerated life test was performed. As shown in Fig. 7a, the cell voltage change of the four PbO$_2$/SS electrodes is about 0.03 V under the same degradation conditions, indicating that the four electrodes are relatively stable in the degradation process. Among them, the cell voltage of PbO$_2$/SS electrode is the highest, while that of Ce-PDMS-PbO$_2$/SS is the lowest, demonstrating that the co-modification of Ce and PDMS reduces the energy consumption in the degradation process of PbO$_2$/SS electrode, and the electrode shows better electrocatalytic performance. To further evaluate the stability of Ce-PDMS-PbO$_2$/SS, the SEM images and XPS spectra of the electrode after 120 min PNP degradation were obtained shown in Figs. S17 and S18. It is obvious that the microsphere structures on the electrode surface are well preserved and the XPS spectra for C 1s, O 1s, Pb 4f, and Ce 3d exhibit nearly no shift compared with those of the initial sample, demonstrating the good structural and chemical stability of Ce-PDMS-PbO$_2$/SS electrode. Fig. 7b displays the time-dependent variation curves of cell voltage for the four PbO$_2$/SS electrodes in 1 M H$_2$SO$_4$ solution with 500 mA cm^{-2} current density during the accelerated life test. The results show that the service life of Ce-PDMS-PbO$_2$/SS electrode doped with Ce and modified by PDMS is prolonged obviously. The accelerated life of Ce-PbO$_2$/SS, PDMS-PbO$_2$/SS, and Ce-PDMS-PbO$_2$/SS electrodes are 21 h, 28 h, and 35 h respectively, which are 1.62, 2.15, and 2.69 times longer than that of unmodified PbO$_2$/SS (13 h). And according to Eq. S5, the actual service lifetimes of the four electrodes were respectively calculated to be 151 d, 244 d, 324 d, and 405 d under the current density of 30 mA cm^{-2}.

Fig. 7. (a) The cell voltage curves of the four PbO_2/SS electrodes in 0.3 M Na_2SO_4 electrolyte containing 50 mg L^{-1} PNP in 120 min; (b) accelerated life test curves measured in 1 M H_2SO_4 solution with the current density of 500 mA cm^{-2} at 25 °C; (c) the bar chart of lead content in the electrolyte after the PNP degradation in 2 h; (d) the curves for the effect of cathode sizes on the degradation efficiency in the degradation system.

The previous SEM images confirmed that compared with the traditional PbO_2/SS electrode, the surface of Ce-doped PDMS-modified PbO_2/SS electrode is denser and its integrity is improved. Therefore, it can effectively prevent the electrolyte from penetrating into the inner part of electrode through cracks and pores, thus delaying the matrix oxide film formation. Besides, compared with the traditional PbO_2/SS, more ·OH free radicals were produced on the Ce-PDMS-PbO_2/SS surface, which inhibited the oxygen evolution in the coating, thus restraining the spalling of the coating. Particularly, for accelerated life measurements, the life loss is owing to the redox reactions in sulfuric acid solution (Eq. 5) [30,68]. Under the condition of constant current accelerated life, the doping of Ce will significantly reduce the cell voltage beneficial to delaying the electrode life. Moreover, it is speculated that the existence of PDMS can hinder the contact between SO_4^{2-} ions and Pb^{4+} sites. The results reveal that Ce doping and PDMS modification for PbO_2/SS effectively restrain the PbO_2 dissolution and improve the service life of Ce-PDMS-PbO_2/SS in an accelerated life test.

$$PbO_2 + H_2O_2 + H_2SO_4 \rightarrow PbSO_4 + 2\,H_2O + O_2 \qquad (5)$$

Furthermore, to study the stability of PbO_2/SS electrodes more systematically, the lead solubility of these four PbO_2/SS electrodes in solution after PNP degradation was analyzed by ICP-AES. The bar chart in Fig. 7c shows the lead content in the simulated wastewater after PNP degradation using four PbO_2/SS electrodes, as can be seen, only a small quantity of PbO_2 is dissolved in the treatment solution. These results demonstrate that the amount of dissolved lead for the modified PbO_2/SS electrodes decreases significantly after the degradation of PNP, which is much lower than the discharge standard of lead-containing wastewater

(≤ 1 mg L^{-1}), and the potential toxicity of lead in the treated water is not significant. Consequently, the stability and security of co-modified electrode Ce-PDMS-PbO_2/SS in water treatment is guaranteed.

3.3.5. Possible degradation pathway of PNP by GC-MS

Many researchers have been involved in the research on the mechanism and pathway of PNP degradation, but a large number of studies have shown that different anode materials will produce various intermediates and degradation pathways when PNP is degraded. Considering that the -NO_2 on PNP can not be removed directly by ·OH attack, the effect of cathode on PNP degradation was studied. Fig. 7d shows the curves for the effect of cathodes with various areas on the PNP degradation efficiency in 60 min. As can be observed that the degradation efficiency of PNP increases gradually with the increase of cathode area, while it increases rapidly when stainless steel ring is employed. This demonstrates that the cathode also plays an important role in the degradation of PNP, such as reducing PNP to p-aminophenol [69]. To verify this idea, GC-MS was applied to detect the intermediates in the PNP degradation process on the Ce-PDMS-PbO_2/SS electrode by mass spectrometry to determine the existing intermediates, so as to speculate the possible degradation path of PNP. The Mass spectrum of the GC-MS peaks at various retention time after electrochemical degradation for 30 min are shown in Fig. S19. Through the analysis of mass spectrometry, the stable intermediates such as p-aminophenol, p-benzoquinone, maleic acid/fumaric acid, propionic acid, malonic acid, acetic acid, etc. are detected, which are listed in Table S4. Based on these results, the possible degradation pathway of PNP is proposed, as illustrated in Fig. 8. Firstly, PNP is reduced to p-aminophenol at the cathode, then p-aminophenol is converted to p-aminobenzoquinone under the attack of
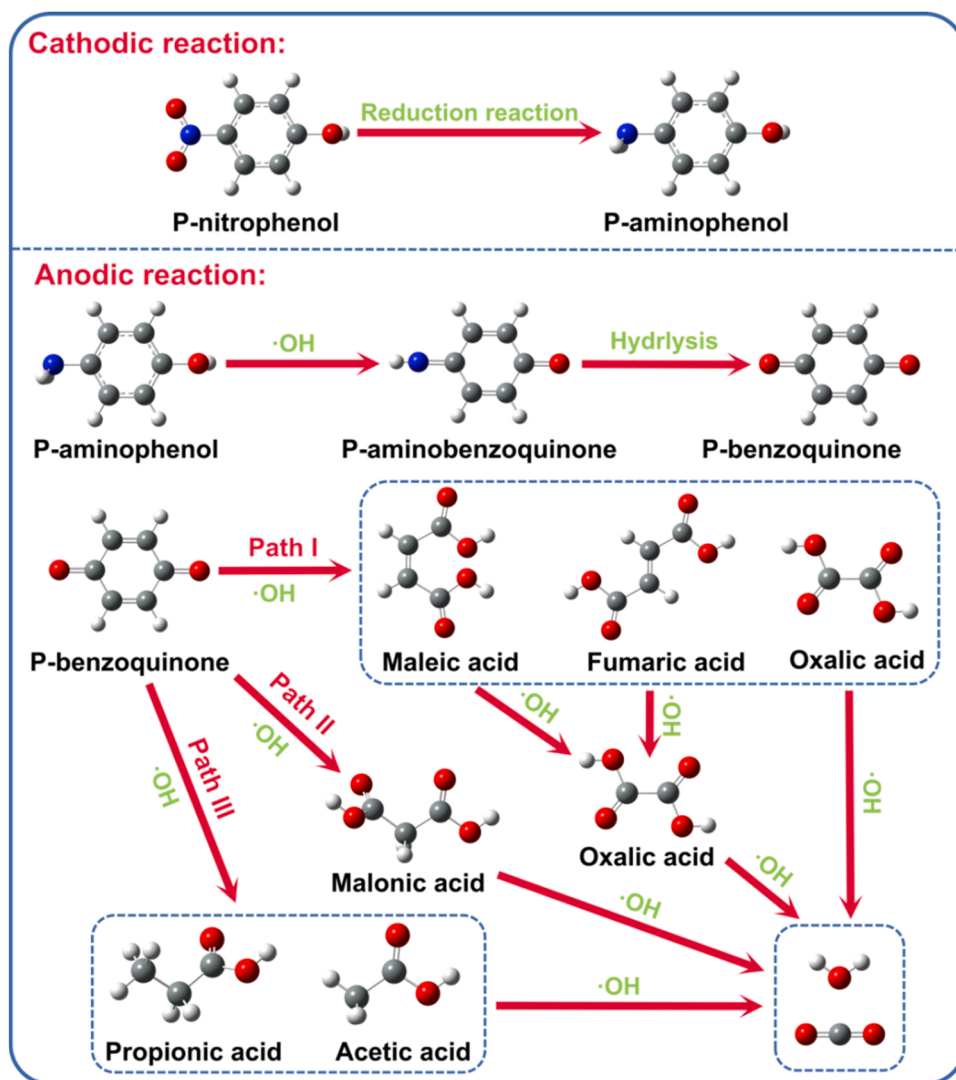
Fig. 8. Possible degradation pathway of PNP on the Ce-PDMS-PbO$_2$/SS electrode in 0.3 M Na$_2$SO$_4$ solution containing 50 mg L^{-1} PNP at 25 ℃.

hydroxyl radicals, and p-aminobenzoquinone is hydrolyzed to p-benzoquinone. And then, the ring-opening reaction of p-benzoquinone occurs under the attack of hydroxyl radicals, and it is speculated that there exist three possible different ring-opening reaction paths. The first reaction path is that p-benzoquinone is first decomposed into fumaric acid/maleic acid and oxalic acid, then further decomposed into oxalic acid, and finally converted into water and carbon dioxide. The second reaction path is that p-benzoquinone is cyclized to malonic acid, and then oxidized to carbon dioxide and water by hydroxyl radicals attack. The third reaction path is that p-benzoquinone is ring-opened and
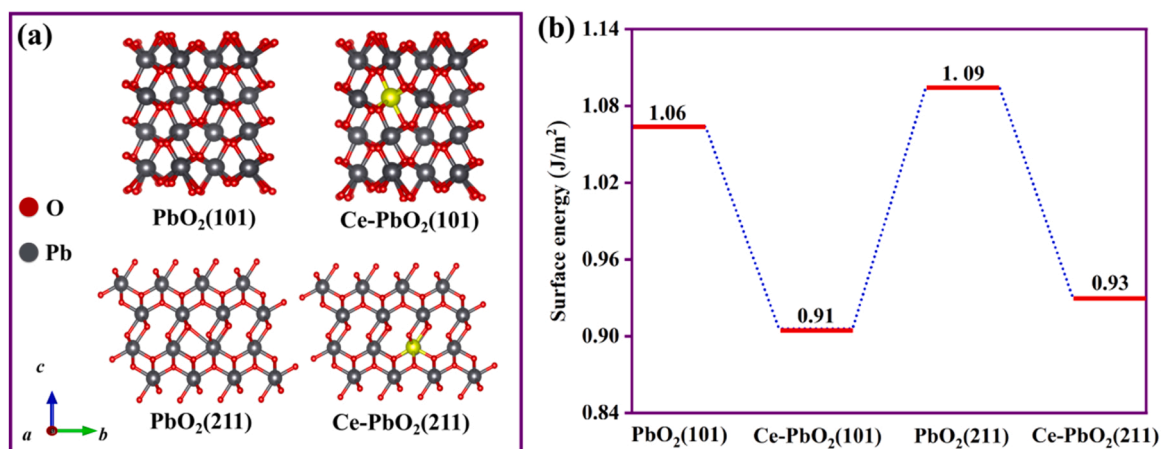

Fig. 9. (101) and (211) crystal plane structure diagrams (a) and the corresponding surface energy step diagrams (b) for PbO$_2$ and Ce-PbO$_2$.

converted to acetic acid and propionic acid, and finally decomposed into carbon dioxide and water.
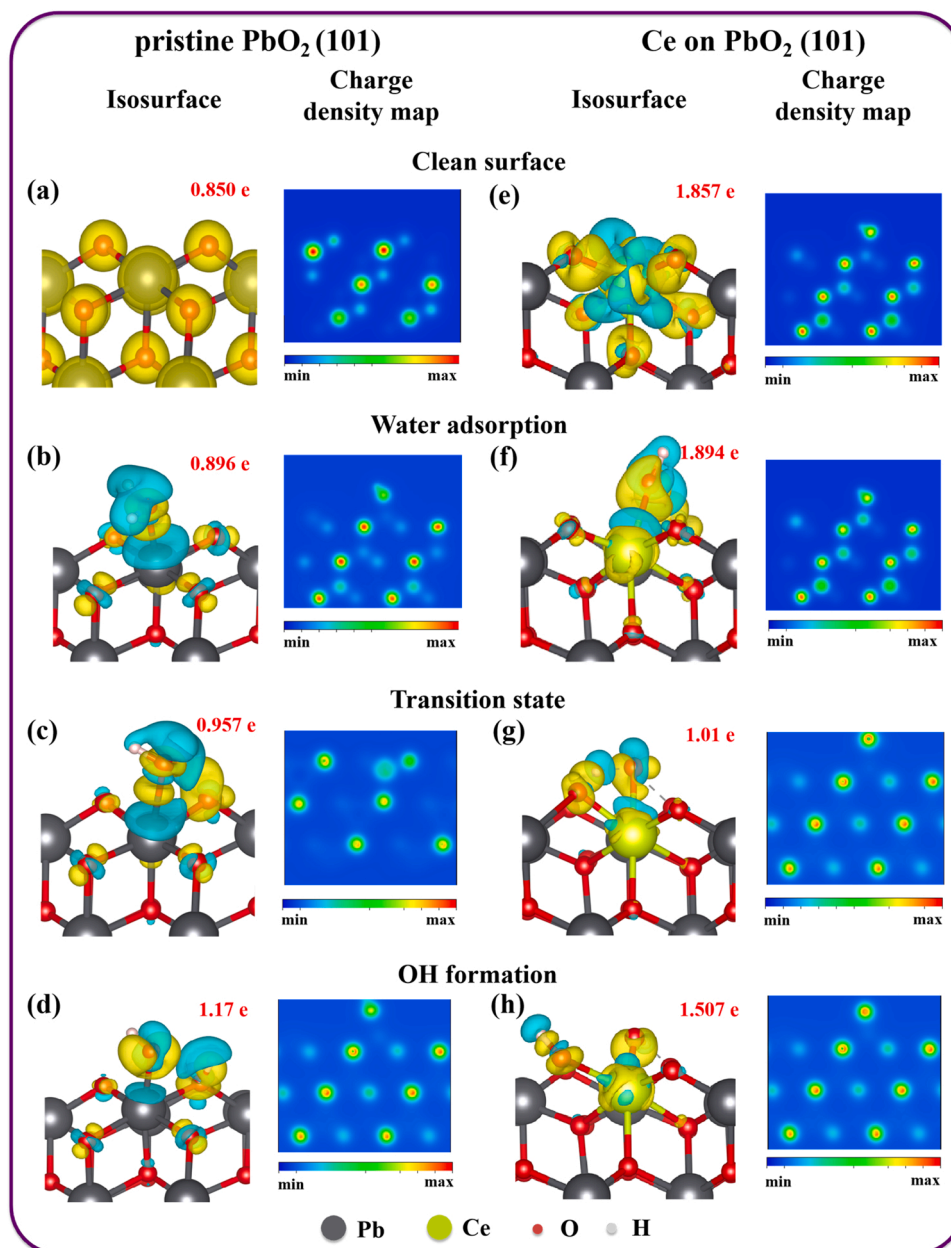
3.4. DFT investigation

3.4.1. Surface energy

As shown in Fig. 9a, the structure diagrams of (101) and (211) crystal planes for PbO_2 and $Ce-PbO_2$ are illustrated. The surface energies of these four crystal planes are calculated theoretically. The relevant parameters are summarized in Table S5, and the results of surface energy for the four crystal planes are demonstrated in Fig. 9b. It can be found that the surface energy 1.09 J/m^2 of the PbO_2 (211) crystal plane is larger than that of PbO_2 (101) crystal plane, indicating that the stable crystal plane is (101) plane before Ce doping, consistent with the experimental results of XRD. The surface energy 0.93 J/m^2 of the Ce-PbO_2 (211) plane is less than or close to that of the Ce-PbO_2 (101) plane, showing that the proportion of PbO_2 (101) plane decreases and that of

the PbO_2 (211) plane increases after Ce doping, which is compatible with the change of PbO_2 plane strength of XRD in the former experiment. After Ce doping, the surface energies of (101) and (211) crystal planes of PbO_2 are reduced to 0.91 J/m^2 and 0.93 J/m^2, suggesting that Ce doping significantly improves the surface activity of PbO_2 beneficial to promoting the formation of ·OH radicals on the surface of PbO_2.

3.4.2. Electronic results

As shown in Fig. S20, the top and side views of the pristine (left side) and Ce doped (right side) PbO_2 (101) $- 2 \times 2$ surface with the four structure states (clean surface, water adsorption, transition state, and ·OH formation) are presented. Moreover, the isosurfaces and charge density maps (CDM) of the four structure states were calculated and plotted, as exhibited in Fig. 10. As illustrated in Fig. 10a, the pristine PbO_2 (101) isosurface exhibits a spherical geometry around the centers of the atom in which the common region matches with the shared charge. As can be seen from Fig. 10b that a small area of shared charge

Fig. 10. Isosurface images and CDM for clean surface (a), (e); water adsorption (b), (f); transition state (c), (g); and ·OH formation state (d), (h) on pristine (left) and Ce doped (right) PbO_2 (101).

between Pb and O can be found for the most stable configuration of water adsorption. Fig. 10c illustrates the transition state, and a shared charge can be observed in the region in close proximity to the water O atom, H, and a surface O atom (HO-H-O$_{surface}$). And as illustrated in Fig. 10d, after the ·OH formation of the H atom bonded to the closest O surface atom, the shared charge region increases can be found. Meanwhile, the isosurfaces and CDM for the four structures of PbO$_2$ (101) after Ce doping are shown in Fig. 10e-f. As displayed in Fig. 10e, a strong interaction between the Ce atom with 4 surface O atoms can be noted. While there only exists a small quantity of shared charge between the surface Pb atom and the water molecule after a water molecule is adsorbed in Fig. 10f. Besides, there appears a shared charge region near by the water O atom, H and Ce atom (HO-H-Ce$_{surface}$) at the transition state (Fig. 10g). As shown in Fig. 10h, after the formation of ·OH, ·OH interacts with the nearest Ce atoms, while H binds to closest O surface atom and is far from ·OH.

Furthermore, the bader charge analysis was employed to analyze the charge transfer and charge population between the active site and the adsorbed intermediate species, and the calculated results are listed in Tables S6 and S7. Previous studies [70,71] have shown that bader charge can often be applied to judge the charge transfer in the adsorption process, so as to judge the strength of adsorption. If there is obvious charge transfer in the adsorption process, there will exist a clear interaction between the active surface and the adsorbed molecules, and the adsorption is likely to be strong; and vice versa. It can be seen from the calculation results that in the four processes of ·OH formation by adsorbing water molecules on the catalyst (101) surface, the positive charges of active oxygen adsorbed by PbO$_2$ (101) are all lower than that of Ce-PbO$_2$ (101), revealing Ce-PbO$_2$ owns a stronger adsorption capacity to the adsorbed intermediate species, which is more beneficial to the formation of ·OH.

3.4.3. Minimum energy pathway (MEP)

To investigate the chemical reactions, the nudged elastic band (NEB) method was employed to calculate the minimum energy pathway (MEP). For this purpose, an initial and a final state have been proposed. First of all, the configuration with a larger adsorption energy of water molecules is applied as the initial state (reactants). While, as a final state (product), ·OH formation through moving one H atom to an adjacent O in the pristine surface or Ce atom is proposed. And the atomic coordinates are completely relaxed in all cases. As shown in Fig. 11, the adsorption NEB images of water on the initial surface (Fig. 11a) and the Ce-doped surface (Fig. 11b) for the formation and desorption process of ·OH are presented. Through the NEB method, the transition state (usually possesses a shorter existence time) and the activation energy barrier to induce the reaction can be found. Consequently, at ·OH formation state on the pristine surface, the activation energy is 1.56 eV, while, the activation energy after Ce doping decreased to 0.66 eV. When Ce exists, this reduction promotes the ·OH formation, in agreement with the previous experimental data. Additionally, the activation energy required for ·OH generation and desorption at the final step was also calculated. After Ce is doped on the surface, the desorption energy of the system is 0.25 eV, while that of the pristine system is only 0.14 eV. All the above analysis results demonstrate that Ce doping could promote the formation of ·OH.

3.4.4. Degradation reaction pathway

The three degradation paths of p-benzoquinone, the key intermediate for the degradation of PNP, are calculated theoretically, and the calculated results are shown in Fig. 12 in the form of free energy step diagram. In order to simplify the calculation process, only one product is selected from each degradation path for theoretical calculation. It can be seen from the results that owing to the ordinate being free energy, each product of path II has the lowest energy and is the most likely to form spontaneously, and the structure of the product formed by this path is stable, thus it is the most suitable path for p-benzoquinone degradation.
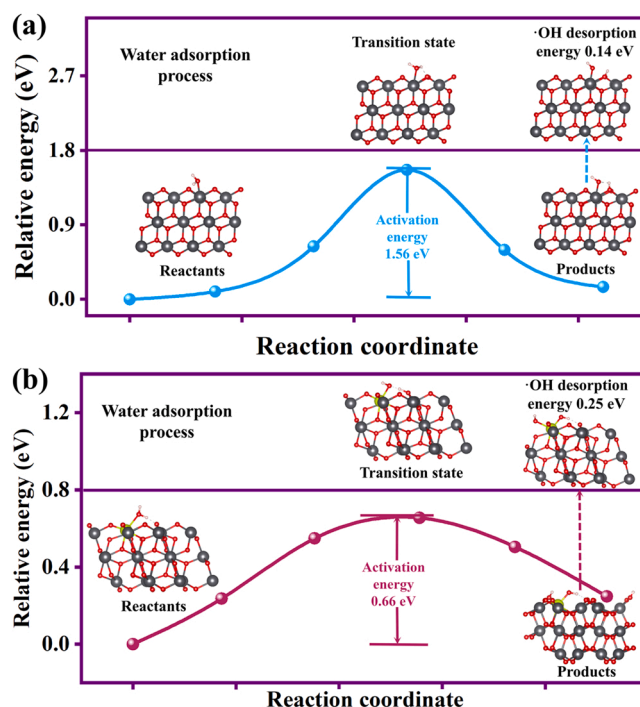
Fig. 11. MEP for water adsorption, ·OH generation and desorption process on (a) pristine PbO$_2$ (101) and (b) Ce-PbO$_2$ (101) calculated with NEB.
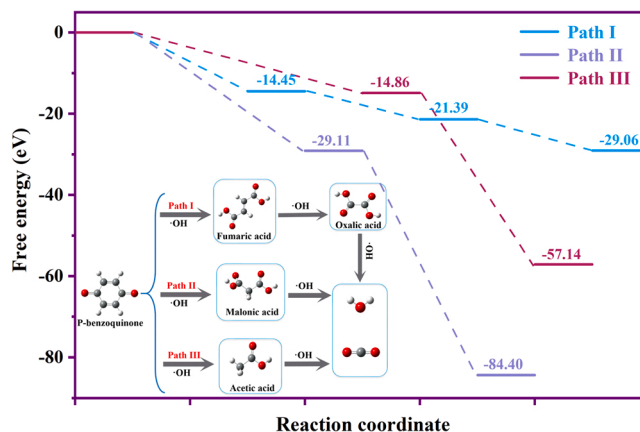

Fig. 12. Free energy step diagram for the three degradation paths of p-benzoquinone.

In addition, the previous calculation results indicate that Ce doping reduces the energy barrier of hydroxyl radical produced by water decomposition, so it is speculated that the degradation path of p-benzoquinone probably is related to the yield of hydroxyl radical. Through the study of the three degradation reaction path, it is found that the degradation process of path II requires the most hydroxyl radicals, which accelerates the ability of p-benzoquinone degradation to produce carbon dioxide and water, while only a small amount of hydroxyl radicals attack p-benzoquinone in other degradation paths, resulting the energy barrier required is higher and p-benzoquinone is more difficult to degrade.

4. Conclusion

To summarize, a novel composite Ce-PDMS-PbO$_2$/SS was directly assembled via ultrasonic-electrodeposition method on stainless steel substrate in lead nitrate solution containing Ce^{3+} and PDMS, and

utilized as the anode for electrocatalytic degradation PNP for the first time. Owing to the remarkable electrochemical performance containing high oxygen evolution potential and exchange current density, low activation energy and charge transfer resistance, and large electroactive area of the Ce-PDMS-PbO$_2$/SS electrode compared with those of the PbO$_2$/SS, Ce-PbO$_2$/SS, and PDMS-PbO$_2$/SS electrodes, the optimal Ce-PDMS-PbO$_2$/SS electrode exhibits an enhanced electrocatalytic degradation performance with the degradation efficiency as high as 96.9% and TOC removal efficiency of 74.9% at 120 min. The electrochemical analysis for PNP degradation results demonstrate that the composite electrode possesses a good adsorption effect on PNP, and the adsorption process controls the degradation process. Contrary to the previous research, the necessity of the cathodic reduction of PNP for PNP degradation was discovered. Accordingly, a convergent paired electrocatalytic degradation mechanism is proposed, that is, the -NO$_2$ groups of PNP reduce to the -NH$_2$ groups at the cathode surface firstly, and then, the cathodically generated p-aminophenol oxidized successively by electrochemically produced ·OH radicals at the anode surface to yield H$_2$O and CO$_2$. Furthermore, the DFT calculation results show that the doping of Ce can reduce the surface energy of the dominant crystal plane of PbO$_2$ and improve the surface catalytic activity of PbO$_2$/SS. Additionally, the doping of Ce could also decrease the activation energy barrier of ·OH and promote the formation of ·OH. The calculation results of the free energy of the degradation process illustrate that p-benzoquinone, the intermediate product of PNP degradation, tends to decompose into malonic acid and then mineralize into water and carbon dioxide.

CRediT authorship contribution statement

Huixi Li: Conceptualization, Investigation, Writing – original draft. **Haoran Wu and Linxia Li:** Data curation, Software. **Wei Zhu:** Investigation. **Shuting Li:** Visualization, Resources. **Qiang Yu:** Validation, Writing review & editing. **Lei Han:** Investigation, Funding acquisition, Writing – review & editing. **Zhen Chen:** Supervision, Conceptualization, Funding acquisition, Writing – review & editing.

Declaration of Competing Interest

The authors declare that they have no known competing financial interests or personal relationships that could have appeared to influence the work reported in this paper.

Data Availability

The data that has been used is confidential.

Supplementary data

Supplementary data related to this article can be found in the online version.

Appendix A. Supporting information

Supplementary data associated with this article can be found in the online version at doi:10.1016/j.apcatb.2023.122884.

References

[1] F. Wang, R. Ou, H. Yu, Y. Lu, J. Qu, S. Zhu, L. Zhang, M. Huo, Photoelectrocatalytic PNP removal using C$_3$N$_4$ nanosheets/α-Fe$_2$O$_3$ nanoarrays photoanode: performance, mechanism and degradation pathways, Appl. Surf. Sci. 565 (2021), 150597.

[2] J. Li, Y. Ren, F. Ji, B. Lai, Heterogeneous catalytic oxidation for the degradation of p-nitrophenol in aqueous solution by persulfate activated with CuFe$_2$O$_4$ magnetic nano-particles, Chem. Eng. J. 324 (2017) 63–73.

[3] J. Yang, B. Pan, H. Li, S. Liao, D. Zhang, M. Wu, B. Xing, Degradation of p-nitrophenol on biochars: role of persistent free radicals, Environ. Sci. Technol. 50 (2016) 694–700.

[4] L. Han, S.G. Liu, J.Y. Liang, Y.J. Ju, N.B. Li, H.Q. Luo, pH-mediated reversible fluorescence nanoswitch based on inner filter effect induced fluorescence quenching for selective and visual detection of 4-nitrophenol, J. Hazard. Mater. 362 (2019) 45–52.

[5] H. Chen, J. Wang, Degradation of sulfamethoxazole by ozonation combined with ionizing radiation, J. Hazard. Mater. 407 (2021), 124377.

[6] D.Q. He, Y.J. Zhang, D.N. Pei, G.X. Huang, C. Liu, J. Li, H.Q. Yu, Degradation of benzoic acid in an advanced oxidation process: the effects of reducing agents, J. Hazard. Mater. 382 (2020), 121090.

[7] R. Song, H. Chi, Q. Ma, D. Li, X. Wang, W. Gao, H. Wang, X. Wang, Z. Li, C. Li, Highly efficient degradation of persistent pollutants with 3D nanocone TiO$_2$-based photoelectrocatalysis, J. Am. Chem. Soc. 143 (2021) 13664–13674.

[8] J. Li, S. Wang, L. Qian, J. Zhang, T. Xu, Y. Li, D. Xu, Supercritical water co-oxidation behavior in the different monohydric alcohol-ammonia reaction environment, Chemosphere 307 (2022), 135858.

[9] Z. Zhang, G. Yi, P. Li, X. Wang, X. Wang, C. Zhang, Y. Zhang, Recent progress in engineering approach towards the design of PbO$_2$-based electrodes for the anodic oxidation of organic pollutants, J. Water Process Eng. 42 (2021), 102173.

[10] Z. Hu, J. Cai, G. Song, Y. Tian, M. Zhou, Anodic oxidation of organic pollutants: anode fabrication, process hybrid and environmental applications, Curr. Opin. Electrochem. 26 (2021), 100659.

[11] M. Shestakova, M. Sillanpää, Electrode materials used for electrochemical oxidation of organic compounds in wastewater, Rev. Environ. Sci. Bio/Technol. 16 (2017) 223–238.

[12] X. Yang, R. Zou, F. Huo, D. Cai, D. Xiao, Preparation and characterization of Ti/SnO$_2$-Sb$_2$O$_3$-Nb$_2$O$_5$/PbO$_2$ thin film as electrode material for the degradation of phenol, J. Hazard. Mater. 164 (2009) 367–373.

[13] H. Jin, X. Zhang, Y. Yu, X. Chen, High-performance Ti/IrO$_2$-RhO$_x$-TiO$_2$/α-PbO$_2$/β-PbO$_2$ electrodes for scale inhibitors degradation, Chem. Eng. J. 435 (2022), 135167.

[14] H. Jing, H. Yang, X. Yu, C. Hu, R. Li, H. Li, Treatment of organic matter and ammonia nitrogen in wastewater by electrocatalytic oxidation: a review of anode material preparation, Environ. Sci.: Water Res. Technol. 8 (2022) 226–248.

[15] Y. Jiang, H. Zhao, J. Liang, L. Yue, T. Li, Y. Luo, Q. Liu, S. Lu, A.M. Asiri, Z. Gong, X. Sun, Anodic oxidation for the degradation of organic pollutants: anode materials, operating conditions and mechanisms. A mini review, Electrochem. Commun. 123 (2021), 106912.

[16] Q. Zhou, X. Zhou, R. Zheng, Z. Liu, J. Wang, Application of lead oxide electrodes in wastewater treatment: A review, Sci. Total Environ. 806 (2022), 150088.

[17] H. Guo, W. Hu, Z. Xu, S. Guo, D. Qiao, X. Wang, H. Xu, W. Yan, How to improve lead dioxide anodes performance in organic wastewater treatment: review and prospect, Process Saf. Environ. Prot. 164 (2022) 189–207.

[18] A. Rahmani, A. Shabanloo, N. Shabanloo, A mini-review of recent progress in lead dioxide electrocatalyst for degradation of toxic organic pollutants, Mater. Today Chem. 27 (2023), 101311.

[19] X. Wang, L. Wang, D. Wu, D. Yuan, H. Ge, X. Wu, PbO$_2$ materials for electrochemical environmental engineering: a review on synthesis and applications, Sci. Total Environ. 855 (2022), 158880.

[20] S. Chen, P. He, X. Wang, F. Xiao, P. Zhou, Q. He, L. Jia, F. Dong, H. Zhang, B. Jia, H. Liu, B. Tang, Co/Sm-modified Ti/PbO$_2$ anode for atrazine degradation: effective electrocatalytic performance and degradation mechanism, Chemosphere 268 (2021), 128799.

[21] Y. Wang, C. Zhou, J. Wu, J. Niu, Insights into the electrochemical degradation of sulfamethoxazole and its metabolite by Ti/SnO$_2$-Sb/Er-PbO$_2$ anode, Chin. Chem. Lett. 31 (2020) 2673–2677.

[22] W. Ji, Y. Wang, Y. Xiong, T.C. Zhang, S. Yuan, Hydrophobic Ce-doped β-PbO$_2$-SDS anode achieving synergistic effects for enhanced electrocatalytic oxidation of As (III), Sep. Purif. Technol. 294 (2022), 121214.

[23] S. Chen, J. Li, L. Liu, Q. He, L. Zhou, T. Yang, X. Wang, P. He, H. Zhang, B. Jia, Fabrication of Co/Pr co-doped Ti/PbO$_2$ anode for efficiently electrocatalytic degradation of beta-naphthoxyacetic acid, Chemosphere 256 (2020), 127139.

[24] Y. Yao, G. Teng, Y. Yang, C. Huang, B. Liu, L. Guo, Electrochemical oxidation of acetamiprid using Yb-doped PbO$_2$ electrodes: electrode characterization, influencing factors and degradation pathways, Sep. Purif. Technol. 211 (2019) 456–466.

[25] Y.-F. Song, J.-M. Liu, F. Ge, X. Huang, Y. Zhang, H.-H. Ge, X.-J. Meng, Y.-Z. Zhao, Influence of Nd-doping on the degradation performance of Ti/Sb-SnO$_2$ electrode, J. Environ. Chem. Eng. 9 (2021), 105409.

[26] S. Chen, J. Chen, Xingyu, G. Xi, X. Zhang, Z. He, Sonoelectrochemical oxidation of aged landfill leachate with high-efficiency Ti/PANI/PDMS-Ce-PbO$_2$ anode, J. Environ. Chem. Eng. 10 (2022), 107499.

[27] Z. Wang, M. Xu, F. Wang, X. Liang, Y. Wei, Y. Hu, C.G. Zhu, W. Fang, Preparation and characterization of a novel Ce doped PbO$_2$ electrode based on NiO modified

Ti/TiO₂ NTs substrate for the electrocatalytic degradation of phenol wastewater, Electrochim. Acta 247 (2017) 535–547.

[28] Z. Lou, J. Wang, S. Wang, Y. Xu, J. Wang, B. Liu, C. Yu, J. Yu, Strong hydrophobic affinity and enhanced •OH generation boost energy-efficient electrochemical destruction of perfluorooctanoic acid on robust ceramic/PbO₂-PTFE anode, Sep. Purif. Technol. 280 (2022) 119919.

[29] G. Zhao, Y. Zhang, Y. Lei, B. Lv, J. Gao, Y. Zhang, D. Li, Fabrication and electrochemical treatment application of a novel lead dioxide anode with super-hydrophobic surfaces, high oxygen evolution potential and oxidation capability, Environ. Sci. Technol. 44 (2010) 1754–1759.

[30] Z. He, J. Zhou, X. Huang, S. Zhang, S. Song, Enhancement of the Activity and Stability of PbO₂ Electrodes by Modifying with Polydimethylsiloxane, J. Electrochem. Soc. 165 (2018) H717–H724.

[31] O.B. Shmychkova, T.V. Luk'yanenko, A.B. Velichenko, R.E. Gladyshevskii, P. Y. Demchenko, R. Amadelli, The influence of deposition conditions on phase composition of lead dioxide-based materials, Prot. Met. Phys. Chem. Surf. 51 (2015) 593–599.

[32] X. Duan, F. Xu, Y. Wang, Y. Chen, L. Chang, Fabrication of a hydrophobic SDBS-PbO₂ anode for electrochemical degradation of nitrobenzene in aqueous solution, Electrochim. Acta 282 (2018) 662–671.

[33] X. Li, H. Xu, W. Yan, Preparation and characterization of PbO₂ electrodes modified with polyvinyl alcohol (PVA), RSC Adv. 6 (2016) 82024–82032.

[34] S. Tong, T. Zhang, Ca Ma, Oxygen evolution behavior of PTFE-F-PbO₂ electrode in H₂SO₄ solution, Chin. J. Chem. Eng. 16 (2008) 885–889.

[35] X. Li, H. Xu, W. Yan, Fabrication and characterization of PbO₂ electrode modified with polyvinylidene fluoride (PVDF), Appl. Surf. Sci. 389 (2016) 278–286.

[36] X. Li, H. Xu, W. Yan, Effects of twelve sodium dodecyl sulfate (SDS) on electro-catalytic performance and stability of PbO₂ electrode, J. Alloy. Compd. 718 (2017) 386–395.

[37] A. Velichenko, T. Luk'yanenko, O. Shmychkova, Lead dioxide-SDS composites: Design and properties, J. Electroanal. Chem. 873 (2020), 114412.

[38] G. Huang, Q. Yang, Q. Xu, S.-H. Yu, H.-L. Jiang, Polydimethylsiloxane coating for a palladium/MOF composite: highly improved catalytic performance by surface hydrophobization, Angew. Chem. -Int. Ed. 128 (2016) 7505–7509.

[39] Y. Yao, C. Zhao, M. Zhao, X. Wang, Electrocatalytic degradation of methylene blue on PbO₂-ZrO₂ nanocomposite electrodes prepared by pulse electrodeposition, J. Hazard. Mater. 263 (2013) 726–734.

[40] G. Hua, X. Zhicheng, Q. Dan, W. Dan, X. Hao, Y. Wei, J. Xiaoliang, Fabrication and characterization of porous titanium-based PbO₂ electrode through the pulse electrodeposition method: Deposition condition optimization by orthogonal experiment, Chemosphere 261 (2020), 128157.

[41] B.G. Pollet, A. Short, Introduction to sonoelectrochemistry, Electrochem. Soc. Interface 27 (2018) 41–42.

[42] V. Saez, M.D. Esclapez, A.J. Frias-Ferrer, P. Bonete, I. Tudela, M.I. Diez-Garcia, J. Gonzalez-Garcia, Lead dioxide film sonoelectrodeposition in acidic media: preparation and performance of stable practical anodes, Ultrason. Sonochem. 18 (2011) 873–880.

[43] C. Wang, T. Zhang, J. Luo, M. Wu, J. Niu, E. Shang, C. Ni, J. Ni, Synergistic enhancement of piezocatalysis and electrochemical oxidation for the degradation of ciprofloxacin by PbO₂ intercalation material, Sep. Purif. Technol. 297 (2022), 121528.

[44] V. Sáez, J. González-García, J. Iniesta, A. Frías-Ferrer, A. Aldaz, Electrodeposition of PbO₂ on glassy carbon electrodes: influence of ultrasound frequency, Electrochem. Commun. 6 (2004) 757–761.

[45] G. Dong, K. Lang, Y. Gao, W. Zhang, D. Guo, J. Li, D.F. Chai, L. Jing, Z. Zhang, Y. Wang, A novel composite anode via immobilizing of Ce-doped PbO₂ on CoTiO₃ for efficiently electrocatalytic degradation of dye, J. Colloid Interface Sci. 608 (2022) 2921–2931.

[46] M. Srisa-Art, Y. Furutani, Simple and rapid fabrication of PDMS microfluidic devices compatible with FTIR microspectroscopy, Bull. Chem. Soc. Jpn. 89 (2016) 195–202.

[47] A. Sabata, W.Jv Ooij, H.K. Yasuda, Plasma-polymerized films of trimet h ylsilane deposited on cold-rolled steel substrates. Part 1. Characterization by XPS, AES and TOF-SIMS, Surf. Interface Anal. 20 (1993) 845–859.

[48] Y.-J. Shih, Y.-H. Huang, C.P. Huang, Oxidation of ammonia in dilute aqueous solutions over graphite-supported α- and β-lead dioxide electrodes (PbO₂@G), Electrochim. Acta 257 (2017) 444–454.

[49] W. Ji, Y. Xiong, Y. Wang, T.C. Zhang, S. Yuan, Multilayered TNAs/SnO₂/PPy/beta-PbO₂ anode achieving boosted electrocatalytic oxidation of As(III), J. Hazard. Mater. 430 (2022) 128449.

[50] S. Anantharaj, S. Noda, M. Driess, P.W. Menezes, The pitfalls of using potentiodynamic polarization curves for tafel analysis in electrocatalytic water splitting, ACS Energy Lett. (2021) 1607–1611.

[51] R. Sanchis-Gual, A. Seijas-Da Silva, M. Coronado-Puchau, T.F. Otero, G. Abellán, E. Coronado, Improving the onset potential and Tafel slope determination of earth-abundant water oxidation electrocatalysts, Electrochim. Acta 388 (2021), 138613.

[52] H. Li, Z. Chen, Q. Yu, W. Zhu, W. Cui, Effects of tungsten carbide on the electrocatalytic activity of PbO₂-WC composite inert anodes during zinc electrowinning, J. Electrochem. Soc. 164 (2017) H1064–H1071.

[53] L. Gui, Z. Chen, B. Chen, Y. Song, Q. Yu, W. Zhu, Q. Hu, Y. Liu, Z. Zheng, L. Ze, H. You, F. Yeasmin, Preparation and characterization of ZnO/PEG-Co(II)-PbO₂ nanocomposite electrode and an investigation of the electrocatalytic degradation of phenol, J. Hazard. Mater. 399 (2020), 123018.

[54] H. Li, C. Zhang, W. Xiang, M.A. Amin, J. Na, S. Wang, J. Yu, Y. Yamauchi, Efficient electrocatalysis for oxygen evolution: W-doped NiFe nanosheets with oxygen vacancies constructed by facile electrodeposition and corrosion, Chem. Eng. J. 452 (2023), 139104.

[55] L. Hui, Y. Xue, B. Huang, H. Yu, C. Zhang, D. Zhang, D. Jia, Y. Zhao, Y. Li, H. Liu, Y. Li, Overall water splitting by graphdiyne-exfoliated and -sandwiched layered double-hydroxide nanosheet arrays, Nat. Commun. 9 (2018) 5309.

[56] Z. Zheng, D. Wu, G. Chen, N. Zhang, H. Wan, X. Liu, R. Ma, Microcrystallization and lattice contraction of NiFe LDHs for enhancing water electrocatalytic oxidation, Carbon Energy 4 (2022) 901–913.

[57] L. Hu, M. Li, X. Wei, H. Wang, Y. Wu, J. Wen, W. Gu, C. Zhu, Modulating interfacial electronic structure of CoNi LDH nanosheets with Ti₃C₂T MXene for enhancing water oxidation catalysis, Int. J. Hydrog. Energy 398 (2020), 125605.

[58] Y. Liu, T. Sun, Q. Su, Y. Tang, X. Xu, M. Akram, B. Jiang, Highly efficient and mild electrochemical degradation of bentazon by nano-diamond doped PbO₂ anode with reduced Ti nanotube as the interlayer, J. Colloid Interface Sci. 575 (2020) 254–264.

[59] X. Duan, Q. Wang, S. Tu, W. Wang, X. Sui, L. Chang, Electrocatalytic degradation of 2,4-dichlorophenol by a 3DG-PbO₂ powdered anode: Experimental and theoretical insights, Sep. Purif. Technol. 282 (2022), 120003.

[60] H. Li, L. Zhang, S. Wang, J. Yu, Accelerated oxygen evolution kinetics on NiFeAl-layered double hydroxide electrocatalysts with defect sites prepared by electrodeposition, Int. J. Hydrog. Energy 44 (2019) 28556–28565.

[61] X. Yang, F. Peng, L. Zhang, X. Wang, S. Liu, W. Yang, L. Zhang, N. Yang, Bimetallic-ZIFs derived quaternary amorphous LDHs decorated with crystalline Ag nanoparticles for highly efficient oxygen evolution reaction, Chem. Eng. J. 449 (2022), 137901.

[62] B. Chen, Q. Yu, Z. Chen, W. Zhu, S. Li, H. You, Z. Lv, Y. Liu, Q. Hu, Z. Zheng, Y. Farhana, Polystyrene microsphere assisted synthesis of a Co/PEG comodified PbO₂ anode and its electrocatalytic oxidation performance, Sep. Purif. Technol. 279 (2021), 119792.

[63] L. Chang, Y. Zhou, X. Duan, W. Liu, D. Xu, Preparation and characterization of carbon nanotube and Bi co-doped PbO₂ electrode, J. Taiwan Inst. Chem. Eng. 45 (2014) 1338–1346.

[64] L. Gui, Z. Chen, Y.Z. Song, W. Zhu, Q. Yu, D. Wu, T. Zheng, Preparation and electrocatalytic performance of nanosphere array PbO₂ electrode on stainless steel-based grid-like ZnO film, J. Electrochem. Soc. 166 (2019) E384–E393.

[65] S.O. Ganiyu, M.G. El-Din, Insight into in-situ radical and non-radical oxidative degradation of organic compounds in complex real matrix during electrooxidation with boron doped diamond electrode: a case study of oil sands process water treatment, Appl. Catal. B: Environ. 279 (2020), 119366.

[66] X. Zhou, Q. Zhou, H. Chen, J. Wang, Z. Liu, R. Zheng, Influence of dimethylphenol isomers on electrochemical degradation: kinetics, intermediates, and DFT calculation, Sci. Total Environ. 794 (2021), 148284.

[67] H. You, Z. Chen, Q. Yu, W. Zhu, B. Chen, Z. Lv, Q. Hu, Y. Liu, Z. Zheng, S. Li, F. Yeasmin, Preparation of a three-dimensional porous PbO₂-CNTs composite electrode and study of the degradation behavior of p-nitrophenol, Sep. Purif. Technol. 276 (2021), 119406.

[68] J. Cao, H. Zhao, F. Cao, J. Zhang, C. Cao, Electrocatalytic degradation of 4-chlor-ophenol on F-doped PbO₂ anodes, Electrochim. Acta 54 (2009) 2595–2602.

[69] P. Jiang, J. Zhou, A. Zhang, Y. Zhong, Electrochemical degradation of p-nitrophenol with different processes, J. Environ. Sci. 22 (2010) 500–506.

[70] T. Ding, X. Liu, Z. Tao, T. Liu, T. Chen, W. Zhang, X. Shen, D. Liu, S. Wang, B. Pang, D. Wu, L. Cao, L. Wang, T. Liu, Y. Li, H. Sheng, M. Zhu, T. Yao, Atomically Precise Dinuclear Site Active toward Electrocatalytic CO₂ Reduction, J. Am. Chem. Soc. 143 (2021) 11317–11324.

[71] B. Zhao, D. Xue, P. Yuan, W. Yan, J. Zhang, S. Mu, J.-N. Zhang, Optimizing electrocatalytic oxygen reduction by adjacent C-O-C structure-driven charge separation on FeN₄ active sites, Appl. Catal. B: Environ. 324 (2023), 122251.